AFRL-RX-WP-TR-2015-0067

VERY LONG WAVE LENGTH IR DETECTORS

Gail J. Brown
AFRL/RXAN

FEBRUARY 2015
Final Report

Distribution Statement A. Approved for public release; distribution unlimited.

See additional restrictions described on inside pages

STINFO COPY

AIR FORCE RESEARCH LABORATORY
MATERIALS AND MANUFACTURING DIRECTORATE
WRIGHT-PATTERSON AIR FORCE BASE, OH 45433-7750
AIR FORCE MATERIEL COMMAND
UNITED STATES AIR FORCE

NOTICE AND SIGNATURE PAGE

Using Government drawings, specifications, or other data included in this document for any purpose other than Government procurement does not in any way obligate the U.S. Government. The fact that the Government formulated or supplied the drawings, specifications, or other data does not license the holder or any other person or corporation; or convey any rights or permission to manufacture, use, or sell any patented invention that may relate to them.

Qualified requestors may obtain copies of this report from the Defense Technical Information Center (DTIC) (http://www.dtic.mil)

AFRL-RX-WP-TR-2015-0067 HAS BEEN REVIEWED AND IS APPROVED FOR PUBLICATION IN ACCORDANCE WITH ASSIGNED DISTRIBUTION STATEMENT.

//SIGNED//
GAIL J. BROWN, Program Mgr
Nanoelectronic Materials Branch
Functional Materials Division

//SIGNED//
DIANA M. CARLIN, Chief
Nanoelectronic Materials Branch
Functional Materials Division

//SIGNED//
KAREN R. OLSON, Deputy Chief
Functional Materials Division
Materials & Manufacturing Directorate

This report is published in the interest of scientific and technical information exchange and its publication does not constitute the Government's approval or disapproval of its ideas or findings.

REPORT DOCUMENTATION PAGE

Form Approved
OMB No. 0704-0188

The public reporting burden for this collection of information is estimated to average 1 hour per response, including the time for reviewing instructions, searching existing data sources, gathering and maintaining the data needed, and completing and reviewing the collection of information. Send comments regarding this burden estimate or any other aspect of this collection of information, including suggestions for reducing this burden, to Department of Defense, Washington Headquarters Services, Directorate for Information Operations and Reports (0704-0188), 1215 Jefferson Davis Highway, Suite 1204, Arlington, VA 22202-4302. Respondents should be aware that notwithstanding any other provision of law, no person shall be subject to any penalty for failing to comply with a collection of information if it does not display a currently valid OMB control number. **PLEASE DO NOT RETURN YOUR FORM TO THE ABOVE ADDRESS**.

1. REPORT DATE ***(DD-MM-YY)***
February 2015

2. REPORT TYPE
Final

3. DATES COVERED ***(From - To)***
1 July 2010 – 16 January 2015

4. TITLE AND SUBTITLE
VERY LONG WAVE LENGTH IR DETECTORS

5a. CONTRACT NUMBER
In-House

5b. GRANT NUMBER

5c. PROGRAM ELEMENT NUMBER
62102F

6. AUTHOR(S)
Gail J. Brown

5d. PROJECT NUMBER
4348

5e. TASK NUMBER

5f. WORK UNIT NUMBER
X0A8 (PS112100)

7. PERFORMING ORGANIZATION NAME(S) AND ADDRESS(ES)
AFRL/RXAN
3005 Hobson Way
Wright-Patterson AFB, OH 45433

8. PERFORMING ORGANIZATION REPORT NUMBER

9. SPONSORING/MONITORING AGENCY NAME(S) AND ADDRESS(ES)
Air Force Research Laboratory
Materials and Manufacturing Directorate
Wright-Patterson Air Force Base, OH 45433-7750
Air Force Materiel Command
United States Air Force

10. SPONSORING/MONITORING AGENCY ACRONYM(S)
AFRL/RXAN

11. SPONSORING/MONITORING AGENCY REPORT NUMBER(S)
AFRL-RX-WP-TR-2015-0067

12. DISTRIBUTION/AVAILABILITY STATEMENT
Distribution Statement A. Approved for public release; distribution is unlimited.

13. SUPPLEMENTARY NOTES
Approved by 88ABW Public Affairs Office: Case number 88ABW-2015-1224 on 19-MAR-2015. Report contains color.

14. ABSTRACT
This overall objective of this research task was to develop an alternative material system for use in VLWIR FPAs with the sensitivity required at 40K for long range sensing and discrimination of cold, dim targets. The alternative material system under development is based on thin alternating layers of indium arsenide and indium gallium antimonide creating a superlattice material capable of infrared detection out to 30 microns. A VLWIR detector adds detection range and discrimination to a space based platform. Operation at 40K provides significant reduction in size, weight and power for this application.

15. SUBJECT TERMS
III-V devices, infrared detection, superlattices, VLWIR detector,

16. SECURITY CLASSIFICATION OF:			17. LIMITATION OF ABSTRACT:	18. NUMBER OF PAGES	19a. NAME OF RESPONSIBLE PERSON (Monitor)
a. REPORT	b. ABSTRACT	c. THIS PAGE			Gail J. Brown
Unclassified	Unclassified	Unclassified	SAR	56	19b. TELEPHONE NUMBER *(Include Area Code)* (937) 255-9854

Standard Form 298 (Rev. 8-98)
Prescribed by ANSI Std. Z39-18

TABLE OF CONTENTS

Section	Page
LIST OF FIGURES	ii
LIST OF TABLES	v
1.0 INTRODUCTION	1
2.0 VERY LONG WAVELENGTH INFRARED DETECTOR MATERIALS RESEARCH PAPERS	2
2.1 Calculation of the Vertical and Horizontal Electron Mobilities in InAs/GaSb Superlattices	2
2.2 Impact of Growth Temperature on InAs/GaInSb Strained Layer Superlattices for Very Long Wavelength Infrared Detection	8
2.3 Quantitative Analysis of Strain Distribution in InAs/$InAs_{(1-x)}Sb_x$ Superlattices	14
2.4 Post Growth Annealing Study on LWIR InAs/GaSb Superlattices	20
2.5 Strain Analysis of Compositionally Tailored Interfaces in InAs/GaSb Superlattices	26
2.6 Optimization of InAs/InGaSb Superlattice Material for Very Long Wavelength Infrared Detection	34
3.0 PUBLICATIONS	45
3.1 Refereed Journal Articles	45
3.2 Conference Proceedings	46
LIST OF ACRONYMS, ABBREVIATIONS, AND SYMBOLS	48

Distribution Statement A. Approved for public release; distribution unlimited.

LIST OF FIGURES

Figure		Page
1	The calculated vertical and horizontal mobilities as a function of InAs layer width for the indicated parameters.	5
2	The calculated perpendicular (continuous) and parallel (dashed) mobilities for four samples for which low-temperature in-plane mobilities (denoted by squares and dashed-dotted lines) are available. The ratio of the mobilities is independent of the assumed value of .	6
3	(a) A HRTEM image of a 47 Å InAs/21.5 Å In0.25GaSb0.75 superlattice showing the first few layers near the substrate. (b) The strain profile of the strain tensor yy along the growth direction averaged parallel to the interface.	10
4	Comparison of the photoresponse spectra of five 47.0 Å InAs/21.5 Å Ga0.75In0.25Sb SL samples grown at 400-450 °C. The insert shows the PR intensity as a function of growth temperature (Tg).	11
5	(a) Temperature dependence of the carrier mobility as a function of T for SL samples grown at 440 (red solid squares) and 390 °C (blue solid triangles). (b) The mobility as a function of growth temperature.	12
6	Time-resolved differential reflectivity data for a ~50 meV 47 Å InAs/21.5 Å In0.25GaSb0.75 superlattice sample at 300 K. The dominant recombination carrier lifetime was measured to be ~70 ns.	13
7	(400) ω-2θ X-ray diffraction scan of the InAs/InAsSb SL with the inset showing the substrate peak and the SL zero-order peak.	16
8	(a) (200) dark-field image of the superlattice, showing the InAs (bright) and the InAsxSb(1-x) (dark), and (b) the intensity profile within the marked region in (a), average parallel to the interfaces, showing grading in the InAs layers.	16
9	A high-resolution TEM image of the superlattice where the bright dots correspond to the projected atomic columns.	17
10	(a) A strain map of the strain tensor εyy, along the growth direction, and (b) a plot of the strain profile, averaged parallel to the interface, within the marked region in (a).	18
11	(a) Profile of the strain tensor εyy (shaded) and the (200) dark-field intensity (black line) averaged over three superlattice periods.	19

Distribution Statement A. Approved for public release; distribution unlimited.

Figure		Page
12	(a) The time-resolved differential transmission decays with model fits for a control 0.5 µm thick 16 MLs InAs/7 MLs GaSb SL sample. The pump fluence ranges from 3-0.6 µJ/cm2. The lowest curve corresponds to an average excess carrier density of 2 x 1016 cm-3. The inset shows the linear dependence of the peak ΔT/T on the excess carrier density. (b) The inverse lifetime vs. excess carrier density for the control (open circles) and annealed SL samples (solid triangles). The minority carrier lifetimes were measured to be 12.0 ns and 15.4 ns for the control and annealed SL samples, respectively and were found as the y-intercept of a linear fit to the data.	23
13	Temperature dependence of (a) the sheet carrier density as a function of 1000/T, and (b) the carrier mobility as a function of T of the unannealed and three annealed SL samples. The measurements on a lightly doped n-type GaSb substrate are included to demonstrate the insignificant impact of the substrate on the SL parameters at low T.	24
14	Comparison of the photoresponse spectra from the control and three annealed SL samples measured at 10K. The annealing temperatures for each sample producing the spectrum are indicated. The small features on the spectra come from water vapor, organic residues and 60 Hz noise spikes.	25
15	X-ray diffraction profiles of the (400) reflection showing the GaSb substrate and the superlattice peaks.	28
16	(a) HAADF-STEM image of the InAs/GaSb superlattice structure, where the arrows indicate position of interfaces. The inset on left is a magnified view of an interface showing well-resolved atomic columns	29
17	Strain analysis of the superlattice with no interface control showing (a) the map of the strain tensor, εyy and (b) a plot of the strain profile averaged parallel to the interface over the whole image in (a).	30
18	Strain analysis of the superlattice with InSb deposition showing (a) the map of the strain tensor, εyy and (b) a plot of the strain profile averaged parallel to the interface over the whole image in (a).	31
19	Strain analysis of the superlattice with Sb2 soaking showing (a) the map of the strain tensor, εyy and (b) a plot of the strain profile averaged parallel to the interface over the whole image in (a). The analysis was performed on HAADF-STEM images acquired with the interfaces viewed along [011].	32
20	Strain analysis of the superlattice with Sb2 soaking showing (a) the map of the strain tensor, εyy and (b) a plot of the strain profile averaged parallel to the interface over the whole image in (a). The analysis was performed on HAADF-STEM images acquired with the interfaces viewed along [0 1¯ 1].	32
21	An X-ray diffraction patterns of a closely lattice matched 68.4 Å period ternary superlattice (SL) sample containing a 0.5 µm thick 47.0 Å InAs/21.5 Å In0.25GaSb0.75Sb SLs. This structure produced the band gap of 46.4 meV or a corresponding onset wavelength of 26.7 µm.	37

Distribution Statement A. Approved for public release; distribution unlimited.

Figure **Page**

22 A HRTEM image of a 47.0 Å InAs/21.5 Å In0.25GaSb0.75Sb superlattices showing the first few layers near the substrate. Inset is a magnified image showing the projected atomic columns along the [011] direction. 37

23 (a) The strain map of an InAs/In0.25Ga0.75Sb superlattices and (b) the strain profile of the strain tensor εyy along the growth direction averaged parallel to the interface within the white box in (a). 38

24 (a) The measured period (black circles) and measured band gap (blue stars), (b) measured net strain (black circles) as a function of the growth temperature (Tg). 39

25 AFM images of 50 µm x 50 µm area scans of 0.5 µm thick 47.0 Å InAs/21.5 Å In0.25Ga0.75Sb superlattices grown at growth temperature (Tg) of 390-470 ºC (from left to right). The value listed on the top (the bottom) of each image represents a Tg (an average root-mean-square roughness). 40

26 (a) Comparison of the photoresponse spectra of five 47.0 Å InAs/21.5 Å In0.25Ga0.75Sb SL samples grown at 400-450 °C. (b) The plot shows the PR intensity as a function of growth temperature (Tg)...41

27 Temperature dependence of (a) the carrier density as a function of 1000/T and (b) the carrier mobility as a function of measurement temperature for SL samples grown at 440 (red solid squares) and 390 °C (blue solid triangles).......................42

28 (a) The carrier density and (b) the mobility as a function of growth temperature measured at 10 K. 43

Distribution Statement A. Approved for public release; distribution unlimited.

LIST OF TABLES

Table **Page**

1 Summary of the measurements results for the sample set. The photoresponse and Hall results are from measurements at 10 K. The cut-off wavelength λc is selected at the point where the intensity drops by 50 %. The PR intensity was measured at 100 meV above the band gap. All of the samples were n-type....10

2 Summary of the measurement results for the sample set. The photoresponse and Hall results are from measurements at 10K. The cut-off wavelength (λc) is selected at the point where the intensity drops by 50%. The PR intensity was measured at 85 meV above the band gap. All of the samples were n-type....24

3 Summary of the measurements results for the sample set. The photoresponse and Hall results are from measurements at 10 K. The cut-off wavelength λc is selected at the point where the intensity drops by 50 %. The PR intensity was measured at 100 meV above the band gap. All of the samples were n-type. The average root-mean-square roughness was based on AFM images of 50 x 50 μm2 area scan. 42

Distribution Statement A. Approved for public release; distribution unlimited.

1.0 INTRODUCTION

The objective of this in-house research program was to develop an alternative material system for use in very long wavelength infrared (VLWIR) focal plane arrays with the sensitivity required at 40K for long range sensing used in space. The alternative material system researched and developed was based on thin alternating layers of indium arsenide (InAs) and indium gallium antimonide (InGaSb) creating a superlattice material capable of infrared detection out to 30 microns. The program utilized a synergistic combination of computational modeling, materials growth, processing, characterization, and performance demonstration to advance the state-of-the art in superlattice materials based on InAs/InGaSb heterostructures. Systematic studies of the molecular beam epitaxial growth and resulting electronic and optical properties were used to optimize the performance of this material system to push the technology closer to the predicted theoretical performance. Computational modeling was used to understand the underlying physics of these materials as well as provide guidance on improved superlattice designs. There were 19 journal articles and 9 proceedings papers written on the research results. The complete listing is at the end of the report.

To capture some of the results accomplished and reported under this research task, selected published papers are incorporated into the report. These selected papers demonstrate the breadth of the effort and highlight different aspects of the research effort. Further details can be explored by reading other papers by the team included in the publication list.

Distribution Statement A. Approved for public release; distribution unlimited.
Approved by 88ABW Public Affairs Office: Case number 88ABW-2015-1224 on 19-MAR-2015.

2.0 Very Long Wavelength Infrared Detector Materials Research

2.1 Calculation of the vertical and horizontal electron mobilities in InAs/GaSb Superlattices

F. Szmulowicz[1] and G. J. Brown[2]
[1]University of Dayton Research Institute, 300 College Park, Dayton, OH 45469-0072
[2]Materials & Manufacturing Directorate, Air Force Research Laboratory, WPAFB, OH 45433-7707

ABSTRACT
Efficient perpendicular transport of carriers by drift and diffusion in InAs/GaSb superlattice-based devices is necessary for achieving high device figures of merit. However, the values of perpendicular mobilities are usually inferred indirectly or through nonstandard experiments. Treating perpendicular and transverse mobilities on equal footing, we present here the results of a calculation of perpendicular and transverse electron mobilities in InAs/GaSb superlattices as limited by interface-roughness scattering. We prove that, in absence of screening, vertical mobilities are generally smaller than horizontal mobilities; with screening, either can be greater than the other. From the mobility curves calculated here for a representative set of samples and roughness parameters, it is possible to infer the value of the vertical mobility from measurements of the horizontal mobility.

INTRODUCTION
The performance of third-generation infrared focal plane arrays and photodiodes based on type-II InAs/GaSb superlattices (SL)[1] requires efficient, vertical transport of photoexcited carriers[2] by drift and diffusion. Unlike horizontal mobilities, vertical mobilities are not measured routinely and are either found from nonstandard and indirect experimental techniques such as geometric magneto-resistance[3] or inferred indirectly from current-voltage data.[4] Here, a consistent a model of horizontal and vertical mobilities as limited by interface roughness scattering is presented. These results can be used to infer the values of vertical mobilities from knowledge of experimentally measured horizontal mobilities and then used in device modeling and for guiding materials development.

Because of the flatness of the heavy-hole bands in the growth direction, charge transport in InAs/GaSb SLs mainly relies on the movement of minority electrons. Electron mobilities are limited by interface roughness scattering (IRS),[5] phonon scattering,[6] and alloy, point, or extended defect scattering.[7] Since the vertical and horizontal transport is limited by the same scattering mechanisms, it should be possible, with the aid of a consistent model, to infer the values of vertical mobilities from the knowledge of experimental horizontal mobilities.

RESULTS AND DISCUSSION
Electron mobilities in InAs/GaSb type-II superlattices are calculated by solving the Boltzmann equation using the scattering rates found by extending the analytical development due to Butcher and Dharssi.[8] First, the electronic structure and wave function of electrons are found by solving the 3x3 envelope function Hamiltonian[9] which accounts for the coupling of the conduction, light-hole, and spin-orbit bands,[10] but in which the parallel and perpendicular motions are decoupled. The Schrodinger equation is solved subject to the periodic boundary conditions, which results in the familiar Kronig-Penney problem for energies. The energy band structure has the form

Distribution Statement A. Approved for public release; distribution unlimited.

$$\varepsilon(\boldsymbol{k}_{//},k_z)=\frac{\hbar^2 k_{//}^2}{2m_{//}}+\varepsilon(k_z) \quad , \tag{1}$$

where $(\boldsymbol{k}_{//},k_z)$ are the parallel and perpendicular wave vectors, $m_{//}$ is the parallel mass, and $\varepsilon(k_z)$ is the solution of the Kronig-Penney problem.[10] The wave function has the form [10]

$$\langle \boldsymbol{r}_{//},z|\boldsymbol{k}_{//},k_z\rangle=\psi_{\boldsymbol{k}}(\boldsymbol{r}_{//},z)=\frac{1}{\sqrt{A}}exp(i\boldsymbol{k}_{//}\bullet\boldsymbol{r}_{//})\phi_{k_z}(z) \quad , \tag{2}$$

where $\phi_{k_z}(z)$ is the cell-periodic Bloch wave with, $-\pi/\ell\le k_z\le\pi/\ell$, ℓ is the superlattice period, and A is the cross-sectional area of the superlattice.

Interface-roughness scattering has been shown to be the main source of low-temperature carrier scattering in InAs/GaSb SLs.[11] Its source are the fluctuation in well width $\Delta(\boldsymbol{r}_{//})$ at position $\boldsymbol{r}_{//}$, with the lateral correlation length of interface fluctuations Λ, which give rise to localized perturbations of height V_0 (GaSb-InAs conduction band offset) at the well/barrier, $z=a$, and barrier/well, $z=-a$, interfaces. Assuming the autocorrelation function of interface fluctuations to be Gaussian, the ensemble-averaged transition rate for scattering between eigenstates $\boldsymbol{k}$ and $\boldsymbol{k}'$ at two equivalent interfaces is given by[12]

$$T(\boldsymbol{k},\boldsymbol{k}')=2\times\frac{2\pi}{\hbar}\left\{\frac{V_0^2\pi\Delta^2\Lambda^2}{A}exp\left(-|\boldsymbol{k}_{//}-\boldsymbol{k}'_{//}|^2\Lambda^2/4\right)|\phi_{k'_z}(a)|^2|\phi_{k_z}(a)|^2\right\}\times\delta(\varepsilon(\boldsymbol{k})-\varepsilon(\boldsymbol{k}')) \quad , \tag{3}$$

which is randomizing[8,13] in k'_z and displays explicit dependence on wave function amplitude.

Using these rates, the Boltzmann equation is solved in the relaxation time approximation for the electron distribution function $f(\boldsymbol{k})$, with the relaxation rate for perpendicular transport given by[14]

$$\frac{1}{\tau_\perp(\varepsilon,k_r)}=\left(\frac{2m_{//}\ell}{\hbar^3}V_0^2|\phi_{k_z}(a)|^2\right)\Delta^2\Lambda^2\left\{\int_0^{\pi/l}dk_z'|\phi_{k_z'}(a)|^2 I_0\left(\frac{\Lambda^2k_r'k_r}{2}\right)exp\left(-\frac{\Lambda^2}{4}(k_r'^2+k_r^2)\right)\Theta(\varepsilon-\varepsilon_z')\right\} \quad , \tag{4}$$

where I_0 is the zeroth order, modified Bessel function of the first kind, $k_r=|\boldsymbol{k}_{//}|$, and Θ is the Heaveside step function. The parallel relaxation rate is given by

$$\frac{1}{\tau_{//}(\boldsymbol{k})}=-\frac{V}{(2\pi)^3}\int d\boldsymbol{k}'\left[1-\frac{k_r'}{k_r}\frac{\tau_{//}(\boldsymbol{k}')}{\tau_{//}(\boldsymbol{k})}cos\,\theta\right]T(\boldsymbol{k},\boldsymbol{k}') \quad , \tag{5}$$

which requires an iterative solution. An iterative solutions is started with the quantum-well limit solution, for which $k_r'=k_r$ (thus, $\tau_{//}(\boldsymbol{k}')=\tau_{//}(\boldsymbol{k})$), so that Equation 5 can be integrated for $\tau_{//}(\varepsilon,k_r)^{-1}$, with I_0 in Equation (4) is replaced by

Distribution Statement A. Approved for public release; distribution unlimited.

$$I_0\left(\frac{\Lambda^2 k'_r k_r}{2}\right) \rightarrow I_0\left(\frac{\Lambda^2 k'_r k_r}{2}\right) - I_1\left(\frac{\Lambda^2 k'_r k_r}{2}\right), \quad (6)$$

where I_1 is the first order, modified Bessel function of the first kind. The mobilities are given by[12,13]

$$\mu_\perp = e\frac{\int \tau_\perp(\boldsymbol{k}) v_\perp^2 \left(\frac{\partial f_0}{\partial E}\right) d\boldsymbol{k}}{\int f_0(\boldsymbol{k}) d\boldsymbol{k}}, \quad (7)$$

$$\mu_{//} == e\frac{\int \tau_{//}(\boldsymbol{k}) v_{//}^2 \left(\frac{\partial f_0}{\partial E}\right) d\boldsymbol{k}}{\int f_0(\boldsymbol{k}) d\boldsymbol{k}}, \quad (8)$$

where the carrier velocity $v(\boldsymbol{k}) = \frac{1}{\hbar}\frac{\partial \varepsilon}{\partial \boldsymbol{k}}$ is obtained from the calculated band structure. Using (6) for transverse relaxation rates, one has that $\tau_{//}(\varepsilon, k_r) \geq \tau_\perp(\varepsilon, k_r)$, so that for isotropic carrier masses $\mu_{//} \geq \mu_\perp$. Importantly, the ratio of the mobilities is independent of Δ.

The ingredients of the calculation are the calculated band structures and wave functions. Interface roughness scattering also depends on the modulus squared of the carrier wave function at the interfaces, Eqs. 3-5 . Mobilities were calculated as a function of superlattice and roughness parameter, with the parallel relaxation rates iterated until converged to 1 part in a million. Figure 1 shows a representative graph calculated without screening for mobilities as a function of InAs layer width. As expected for interface roughness scattering, the calculated mobilities increase with InAs layer width and, as deduced earlier, $\mu_{//} \geq \mu_\perp$. At around 60 Å the electron level falls below the top of the valence band in the GaSb barrier material, which allows the electron to tunnel through GaSb partially as a light hole, which explains the change in the slope at that InAs width. As a function of GaSb layer width (not shown), the calculated mobilities decrease with increasing GaSb layer width since the electron wave function cannot penetrate into the barrier material and is more susceptible to InAs layer width fluctuations; perpendicular mobilities also decrease because the carrier mass increases with superlattice period.

Distribution Statement A. Approved for public release; distribution unlimited.

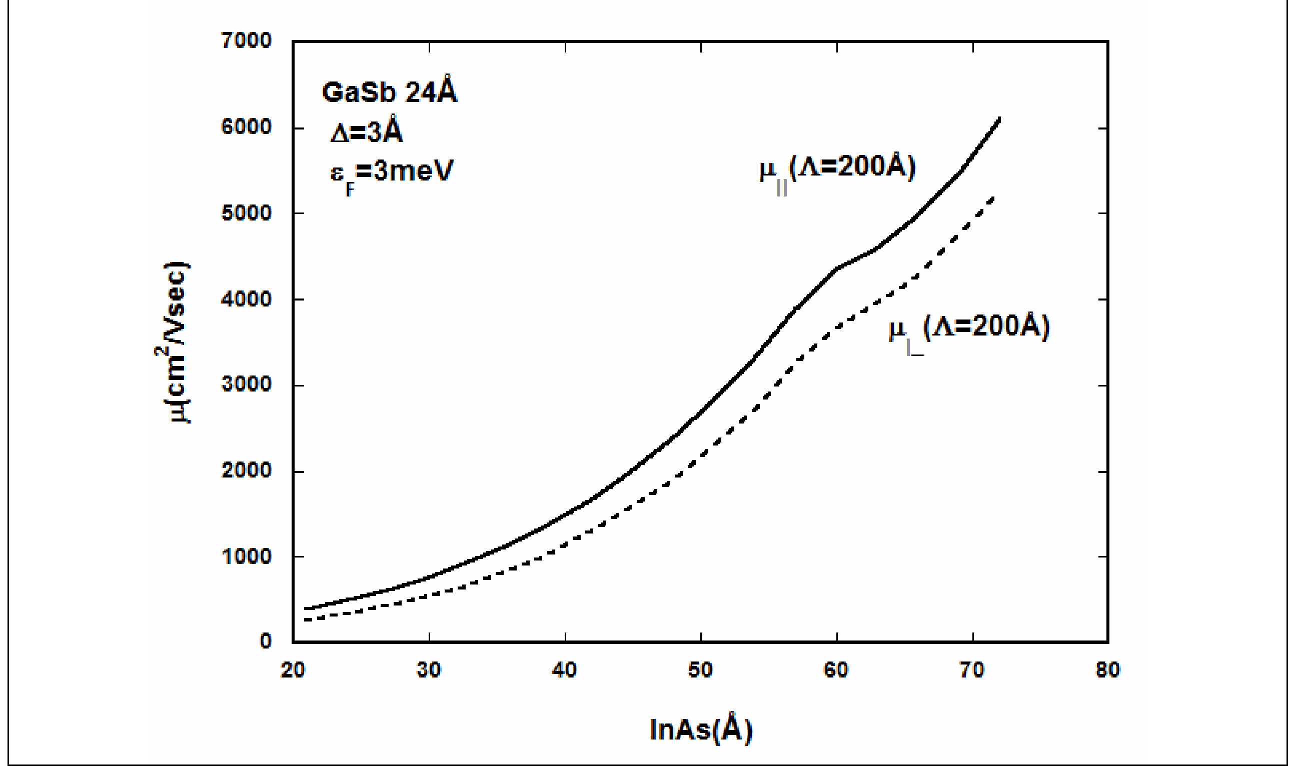

Figure 1. The calculated vertical and horizontal mobilities as a function of InAs layer width for the indicated parameters.

However, interface roughness scattering is screened by the free electrons, which reduces scattering rates and enhances mobilities. Adopting Thomas-Fermi screening, the transition matrix is multiplied by the screening factor[15,16]

$$S_C(q)=\left(\frac{q}{q+q_s}\right)^2=\left(\frac{|\boldsymbol{k}_{//}-\boldsymbol{k}'_{//}|}{|\boldsymbol{k}_{//}-\boldsymbol{k}'_{//}|+q_s}\right)^2=\left(\frac{\sqrt{k_r^2-2k_rk'_r\cos\theta'+k_r'^2}}{\sqrt{k_r^2-2k_rk'_r\cos\theta'+k_r'^2}+q_s}\right)^2, \qquad (9)$$

where $|\boldsymbol{k}_{//}-\boldsymbol{k}'_{//}|$ is the parallel momentum transfer and q_s is the Thomas-Fermi screening length, a number on the order of 180 Å. Note that screening is largest for backward scattering, $\theta'=\pi$, for which the factor $1-(k'_r/k_r)\cos\theta'=1+(k'_r/k_r)$ in Equation 5 is also the largest. Hence, screening accentuates parallel rates with respect to perpendicular rates, making it is possible for perpendicular mobilities to be larger than horizontal mobilities.

We use the roughness parameters (Δ,Λ) to fit the measured horizontal mobilities and then calculate them to calculate the perpendicular mobilities. In Figure 2, we show a fit to the horizontal mobilities of four n-type InAs/GaSb SL samples studied earlier. [17] Using the experimentally measured carrier concentrations [17] on the order of 3.0 x10^{10} cm^{-2} and the calculated band structure, the Fermi energies for the four samples were found to be between 15.6 and 19.5 meV. Taking the vertical roughness parameter for the widest sample to be Δ= 1 ML (monolayer), its horizontal mobility was fit with the correlation length Λ=225 Å, a number that is of the same order of magnitude as measured by STM by Lew et al.,[18] who found (Δ=1.9±0.1

Distribution Statement A. Approved for public release; distribution unlimited.

Å, Λ=112±16 Å; Δ=2.8±0.2 Å, Λ=174±21 Å) for InAs on InGaSb and (Δ=3.2±0.2 Å, Λ=301±39 Å; Δ=4.3±0.2 Å, Λ=327±38 Å) for InGaSb on InAs interfaces in (110)/(1-10) cross-sections. Using this value of Λ for the rest of the samples, the corresponding values of Δ were also on the order of 1 ML except for the narrowest sample in the study, for which Δ was on the order of 2 ML (observe that for both mobilities $\mu \propto \Delta^2$). These values were then used to calculate the corresponding vertical mobilities, as shown in Figure 2.

Figure 2 shows that as in quantum wells[19] the horizontal mobility is a double-valued function of Λ, with the minimum corresponding to the value of Λ comparable to the Fermi wavelength. For the values of the fitted (Δ, Λ) pairs, the perpendicular mobilities are about half the horizontal mobilities; however, these ratios are very sensitive to the value of Λ but are independent of Δ. Curves like those in Figure 2 make it possible to find the values of perpendicular mobilities given the measured value of the corresponding horizontal mobility.

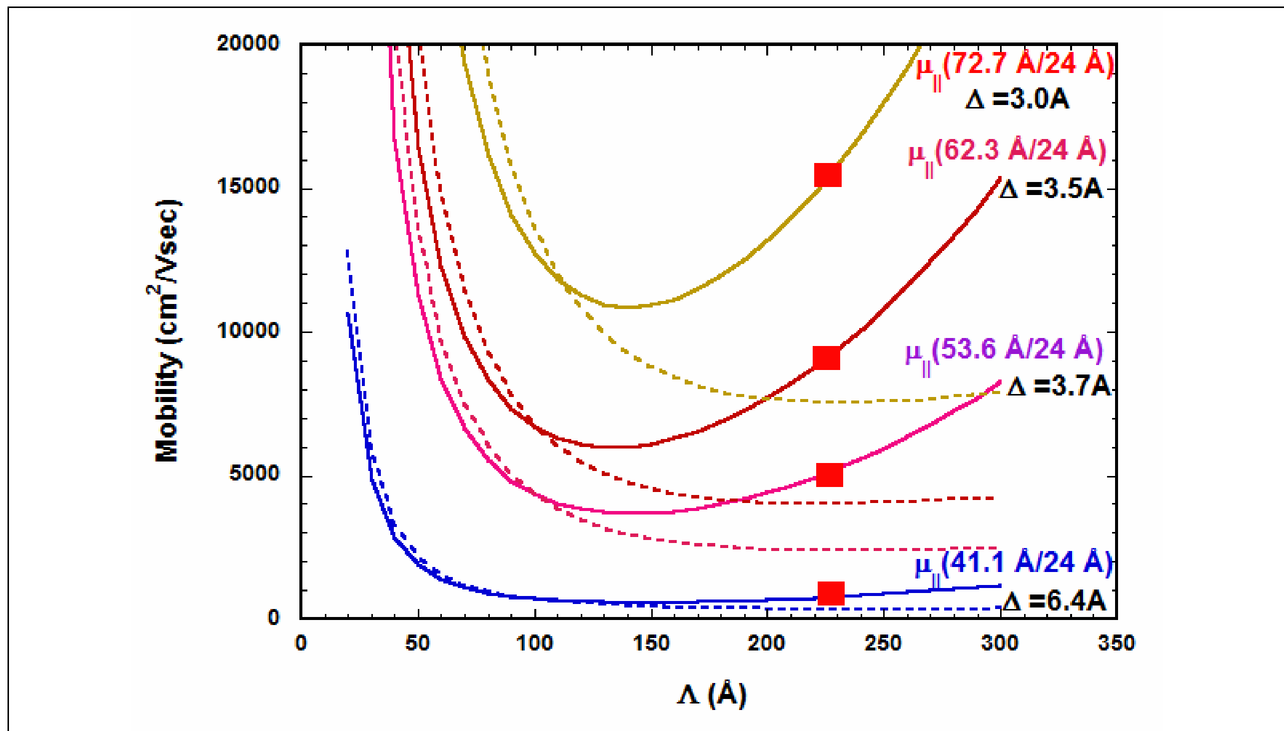

Figure 2. The calculated perpendicular (continuous) and parallel (dashed) mobilities for four samples for which low-temperature in-plane mobilities (denoted by squares and dashed-dotted lines) are available. The ratio of the mobilities is independent of the assumed value of Δ.

CONCLUSION

The vertical and horizontal interface roughness scattering-limited mobilities in InAs/GaSb superlattices have been calculated by solving the corresponding Boltzmann equation, using the energy spectra and wave functions obtained from the solution of a coupled envelope-function Hamiltonian for the superlattice. Both mobilities are treated on equal footing, using the same model for interface roughness scattering transition rates, which makes it possible to compare the two. The calculated mobilities are strong functions of the interface roughness parameters and of

Distribution Statement A. Approved for public release; distribution unlimited.

carrier screening. In absence of screening, a theorem was derived that shows that vertical mobilities are generally smaller than horizontal mobilities. With screening included, backward scattering in horizontal transport is accentuated, so that no general predictions can be made. Using present results and the measured values of horizontal mobilities, it possible to estimate the corresponding vertical mobilities for use in detector modeling and materials optimization.

REFERENCES:

1. A. Rogalski, J. Antoszewski, and L. Faraone, J. Appl. Phys. **105**, 091101 (2009).
2. Y. Cuminal., J. B. Rodriguez, and P. Christol, Fin. El. Anal. and Design **44**, 611 (2008).
3. F. Aristone, J.-C. Portal, J. F., Palmier, and J. C. Harmand, Brazilian J. Physics **29**, 375 (1999); F. Aristone, P. Gassot, J. F. Palmier, D. K. Maude, B. Goutiers, J. L. Gauffier, J. C. Portal, and G. Mollot, Superlattices Microstruct. 1**5,** 225(1994).
4. L. Bürkle, L., F. Fuchs, R. Kiefer, W. Pletschen, R. E. Sah, and J. Schmits, Mater. Res. Soc. Symp. Proc. **607,** 77 (2000).
5. C. A. Hoffman, J. R. Meyer, E. R. Youngdale, F. J. Bartoli, and R. H. Miles, Appl. Phys. Lett. **63**, 2210 (1993).
6. J. F. Palmier and A. Chomette, J. Physique **43**, 381 (1982).
7. T. Ando, J. Phys. Soc. Jpn. **51**, 3900 (1982).
8. I. Dharssi, and P. N. Butcher, J. Phys. Condens. Matter **2**, 4629 (1990).
9. G. Bastard, *Wave Mechanics Applied to Semiconductor Heterostructures* (Halsted, New York 1988).
10. F. Szmulowicz, E. R. Heller, and K. Fisher, Superlattices and Microstructures **17**, 373 (1995).
11. J. R. Meyer, D. J. Arnold, C. A. Hoffman, and F. J. Bartoli, App. Phys. Lett. **58**, 2523 (1991).
12. B. R. Nag, *Electron Transport in Compound Semiconductors* (Springer, New York, 1980); the model can also treat nonequivalent interfaces.
13. B. R. Nag, *Theory of Electrical Transport in Semiconductors* (Pergamon, New York,1972).
14. G. Etemadi and J. F. Palmier, Solid State Commun. **86**, 739(1993).
15. D. A. Broido and T. L. Reinecke, Phys. Rev. B **64**, 045324 (2001).
16. T. Ando, A. B. Fowler, and F. Stern, Rev. Mod. Phys. **54**, 437 (1982).
17. F. Szmulowicz, S. Elhamri, H. J. Haugan, G. J. Brown, and W. C. Mitchel, J. Appl. Phys. **101**, 043706 (2007); J. Appl. Phys. **105**, 074393 (2009).
18. A.Y. Yew, S.L. Zuo, E.T. Yu, and R.H. Miles, Appl. Phys. Lett. 70, 75 (1997); Phys. Rev. B **57**, 6534 (1998).
19. A. Gold, Phys. Rev. B **35**, 723 (1987).

Distribution Statement A. Approved for public release; distribution unlimited.

2.2 Impact of growth temperature on InAs/GaInSb strained layer superlattices for very long wavelength infrared detection

H. J. Haugan,[1, a)] G. J. Brown,[1] S. Elhamri,[2] W. C. Mitchel,[1] K. Mahalingam,[1] M. Kim,[1] G. T. Noe,[3] N. E. Ogden,[3] and J. Kono[3]
[1]Air Force Research Laboratory, Materials & Manufacturing Directorate, Wright-Patterson Air Force Base, Ohio 45433, USA
[2]Department of Physics, University of Dayton, Ohio 45469, USA
[3]Department of Electrical and Computer Engineering, Rice University, Houston, Texas 77005, USA

ABSTRACT
We explore the optimum growth space for a superlattice (SL) structure of 47.0 Å InAs/21.5 Å $Ga_{0.75}In_{0.25}Sb$ designed for the maximum Auger suppression for a very long wavelength infrared gap. Our growth process to create this SL structure produces a consistent band gap of 50±5 meV. However SL quality assessed by photoresponse (PR) intensity is very sensitive to the growth temperature (T_g). For the SLs grown at 390-470 °C, a PR signal gradually increases as T_g increases from 400 to 440 °C with a maximum at 440 ºC. Outside this temperature window, the SL quality deteriorates very rapidly. All SLs were residual n-type with mobility of ~10,000 V/cm^2 and 300 K recombination lifetime of ~70 ns for an optimized SL.

INTRODUCTION
An alternative infrared material system proposed by Smith and Mailhiot[1] uses the concept of broken-gap type-II band alignment of the InAs/GaInSb strained layer superlattices (SLs) to achieve narrow gaps for the very long wavelength infrared (VLWIR) detection (>14 µm). By alloying indium to the GaSb layer, the lattice constant of the GaInSb layer increases. The biaxial tension in the InAs layer lowers the conduction band, while the biaxial compression in the GaInAs layer raises the heavy-hole (HH) band. As a result, the very narrow gap can be achieved without sacrificing optical absorption. In addition, an intentionally introduced strain can create a large splitting between the HH and light-hole bands in the p-type SLs; this situation can prevent the hole-hole Auger recombination process, therefore the Auger limited minority carrier lifetime, detectivity, and the background limited operating temperature can be significantly improved. Grein et. al.[2] demonstrated how a small variation in the strain splitting between the uppermost valence bands can create an order of magnitude differences on their calculated detectivities. For the SLs designed for the same 80 meV gap at 40 K, the electronic band structure of either 49.7 Å InAs/57.0 Å $Ga_{0.9}In_{0.1}Sb$ or 47.0 Å InAs/21 .5 Å $Ga_{0.75}In_{0.25}Sb$ SL designs computed with the interface terms had the total lifetime of either $5x10^{-9}$ or $1.4x10^{-7}$ seconds. This difference leads the device detectivity to be either $5.2x10^{13}$ or $6.0x10^{14}$ cmHz^{½}/W. Although the greater strain splitting generates the better detectivity, one has to limit the indium alloy composition below 30% due to difficulties in strain balancing above this percentage. The authors also computed device detectivity for the more realistic case of 82 meV SL detectors with a 35 ns Shockley-Read-Hall (SRH) lifetime.[3] Unexpectedly, Auger processes were fast enough to overrule SRH processes, and the detectors still can operate at reasonably high temperatures, roughly exceeding 150 K.[3] Therefore, strained InAs/GaInSb SL system appeared to be an excellent choice for the VLWIR detection. Unfortunately, the VLWIR InAs/GaInSb material growth studies are still in immature stage of development. Many crystal growers tend to believe that the existence of an alloy layer can create a higher degree of disorder caused by alloy scattering, indium segregation,

Distribution Statement A. Approved for public release; distribution unlimited.

compositional interdiffusion, and unpredictable others. Therefore controlling a precise gap and achieving high quality of materials using the ternary system can be more difficult than using the binary. So far, a majority of reported VLWIR photodiodes covering 50 % cutoff wavelengths from 15 to 26 μm at 10 K in the past years were based on minimally strained binary SL materials.[4-7] Although there was a report of a ternary SL photodiode with a 50 % cutoff wavelength of 21 μm at 40 K using a 29 MLs InAs/10 MLs $Ga_{0.93}In_{0.07}Sb$ SLs with 1 ML of InSb-like interfacial bonds,[8] the authors added very little indium to their design and could not take advantages of alloying indium to the GaSb layer to improve Auger lifetimes. Therefore, their detectivity was about $3x10^9$ $cmHz^{½}/W$ at 40 K.

In this letter, we report ternary growth studies to develop this material for VLWIR detection. We select a SL structure of 47.0 Å InAs/21.5 Å $Ga_{0.75}In_{0.25}Sb$ proposed by Grein et. al.,[2] theoretically adjusted for the greatest possible detectivity, and optimize a growth parameter for the best possible material quality. Since SL material quality is strongly related to the densities of nonradiative SRH recombination centers and the residual dopings, the impact of growth temperature (T_g) on the photoresponse (PR) intensity, the charge carrier density and mobility, and the recombination lifetimes will be investigated using photoconductivity, temperature-dependent Hall effect, and time-resolved pump-probe measurements.

The ternary SLs were grown by molecular beam epitaxy using elemental metals for Ga and In, and valved cracker cells for As and Sb. The repeated SL stack and buffer layer were deposited on a lightly doped n-type GaSb (100) wafer, which provides a high enough resistivity substrate for electrical measurements.[9] A series of 0.5 μm thick 47.0 Å InAs/21.5 Å $Ga_{0.75}In_{0.25}Sb$ SLs were grown at T_g between 390 and 470 °C. To grow the intended sample structure, the growth rate combination of 1.20, 0.33, and 0.40 Å/s was used for GaSb, InAs, and InSb, respectively. The V/III flux ratio was set at minimum of 3 for both InAs and GaSb layers. Since monomeric Sb is the species critical to reducing densities of SRH recombination centers in the SL material, we set a cracking zone temperature at 950 ºC for the series, which is close to the suggested value by the EPI Model 200 cc Mark V Corrosive Series Valved Cracker. Interface between InAs and GaInSb layer was not intentionally controlled in order to compensate the residual strain in the SLs. Therefore, the strain of the SLs varied between +0.2 and 0.0 %. Structural properties of grown samples such as SL period, residual strain, and overall layer thickness were assessed by high-resolution transmission electron microscopy (HRTEM) and high-resolution X-ray rocking curve (HRXRC) measurements. Figure 3a is a HRTEM image of a 47 Å InAs/21.5 Å $In_{0.25}Ga_{0.75}Sb$ SLs showing the first few SL periods adjacent to the substrate, wherein the amplitude contrast is optimized to delineate the individual layers in the structure. The average values for the individual layer thicknesses of InAs and GaInSb measured from this image were 45.7 Å ± 0.4 Å and 22.8 Å ± 1.6 Å, which are close to their respective intended values of 47.0 Å and 21.5 Å. In addition, quantitative strain analysis of these images was also performed using procedures described in a previous report.[10] Figure 3b shows the profile of the strain tensor $_{yy}$ normal to the growth direction, averaged along the interface. Sharp negative spikes at the GaInSb-on-InAs interface (denoted by arrows) are clearly observed, indicating that this interface is in tensile strain and that the dominant bond type at this interface is Ga-As. On the other hand the regions corresponding to the InAs-on-GaInSb interface exhibits strain inversion so that the overall strain at this interface is small. It is also observed that the GaInSb layers exhibit a strong compressive strain of approximately 0.03, which is consistent with the high indium in this

Distribution Statement A. Approved for public release; distribution unlimited.

sample. Further analysis indicated that the net strain over several periods examined is to be about 0.0005. With the measured period of 68.4 Å strain balanced SL structure, we obtained the band gap of 45.3 meV or a corresponding onset wavelength of 26.4 µm. The measured periods and strains of the growth temperature study series are listed in Table 1.

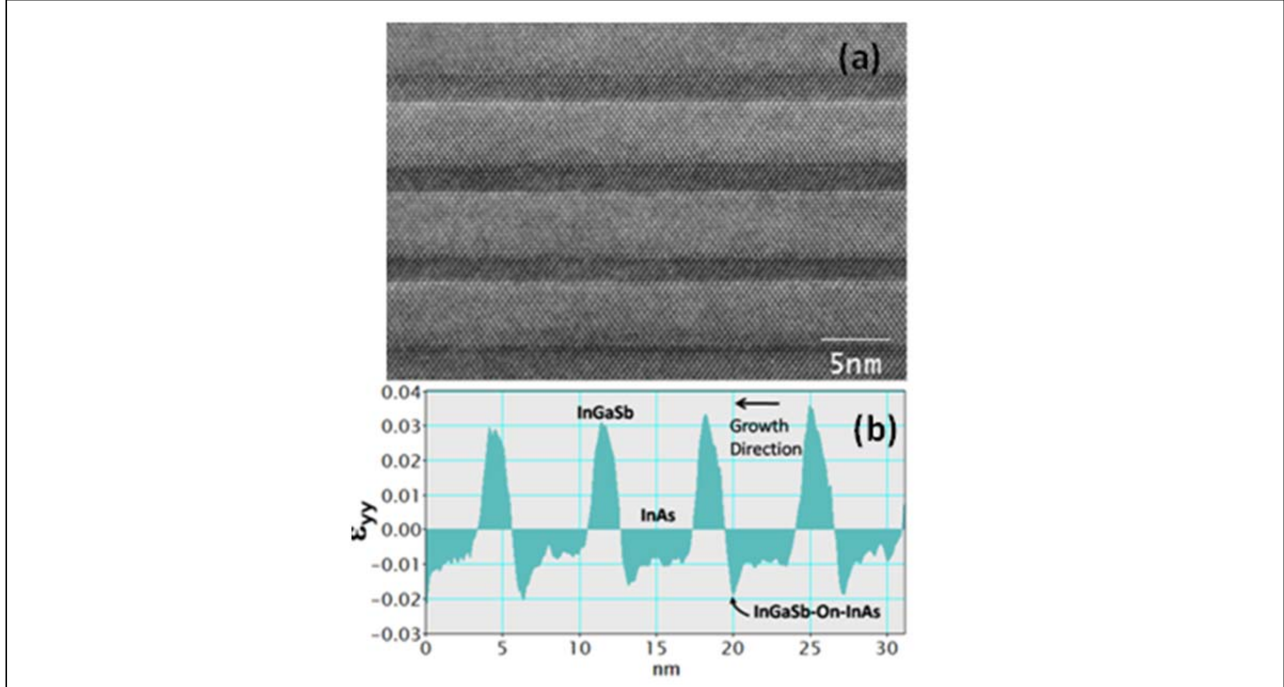

Figure 3. (a) A HRTEM image of a 47 Å InAs/21.5 Å $In_{0.25}GaSb_{0.75}$ superlattice showing the first few layers near the substrate. (b) The strain profile of the strain tensor ε_{yy} along the growth direction averaged parallel to the interface.

Table 1. Summary of the measurements results for the sample set. The photoresponse and Hall results are from measurements at 10 K. The cut-off wavelength λ_c is selected at the point where the intensity drops by 50 %. The PR intensity was measured at 100 meV above the band gap. All of the samples were n-type.

Sample	T_g (^oC)	P (Å)	ε (%)	E_g (meV)	λ_c (µm)	PR intensity (arb. units)	Carrier (cm^{-2})	Mobility (cm^2/Vs)
SL1	390	67.8	+0.18	X	X	X	9.1 E +11	6073
SL2	400	68.5	+0.17	47.0	19.0	0.08	8.9 E+11	9887
SL3	410	67.5	+0.17	43.8	20.1	0.32	7.1 E+11	11286
SL4	430	68.0	+0.17	46.0	19.0	0.59	6.4 E+11	10502
SL5	440	67.5	+0.16	53.0	17.0	1.09	5.2 E+11	9950
SL6	450	68.6	+0.16	50.0	16.2	0.07	5.6 E+11	8529
SL7	460	67.7	+0.11	60.0	15.7	0.06	2.8 E+13	112
SL8	470	67.5	+0.00	X	X	X	1.2 E+14	21

Distribution Statement A. Approved for public release; distribution unlimited.

Since the strength of PR signal is a strong function of the overall material quality, PR spectra were used to identify the spectral range of the material and strength of the optically excited signal. The spectra were collected with a Fourier Transform Infrared spectrometer at a temperature of 10 K. Due to the relatively low resistivity of the samples, the photoconductivity was measured in the current biased mode, with a current of 0.5 mA between two parallel strip contacts on the surface. Figure 4 shows the five PR spectra collected from the sample set with varying T_g of 400, 410, 430, 440, and 450 ºC. Although the PR intensities are given in arbitrary units, the relative signal strengths can still be compared as the test conditions for all the samples were kept constant. We observe that the band gap energies of all SLs in this series are around 50 ±5 meV, while PR intensity gradually increases as T_g increases from 400 to 440 ºC by reaching a maximum at 440 ºC, and then drops by over an order of magnitude at higher temperatures. This result indicates that while our MBE growth process used can reproduce a consistent gap near 50 meV within a range of few meV. However the PR intensity can be very sensitive to the minor variations of material quality. We observe a shallow growth window of 410-440 ºC for given V fluxes and cracking zone temperatures we used. Outside this temperature window, the material quality deteriorates very rapidly.

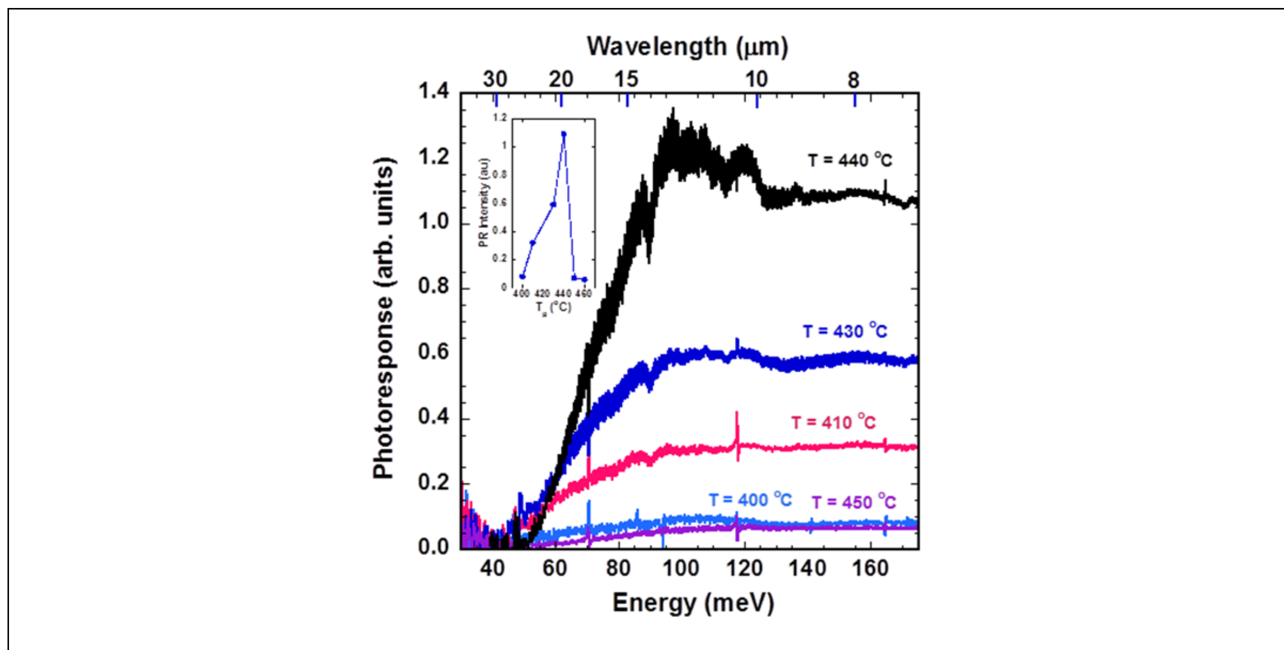

Figure 4. Comparison of the photoresponse spectra of five 47.0 Å InAs/21.5 Å $Ga_{0.75}In_{0.25}Sb$ SL samples grown at 400-450 °C. The insert shows the PR intensity as a function of growth temperature (T_g).

To investigate transport properties, variable temperature resistivity and Hall effect measurements were performed on each sample in this set. The temperature dependence of the in-plane mobility for two SLs is shown in Figure 5a, where the mobility is relatively temperature insensitive up to roughly 70 K. The 10 K carrier density and mobility, along with the corresponding T_g, for each sample are listed in Table 1. The impact of growth temperature on the carrier mobility is summarized on Table 1, and illustrated in Figure 5b. The mobility increases from 6,000 to 11,300 cm^2/Vs as T_g increases from 390 to 410 ºC, gradually decreases to 8500 cm^2/Vs as T_g

Distribution Statement A. Approved for public release; distribution unlimited.

increases to 450 ºC, and then drops significantly for the two highest T_g of 460 and 470 ºC. The background carrier density gradually decreases, reaching a minimum of 5.2 x 10^{11} cm^{-2} at 440 ºC, with a corresponding mobility of roughly 10,000 cm^2/Vs. Based on the transport data, transport properties rapidly deteriorate for T_g above 450 ºC.

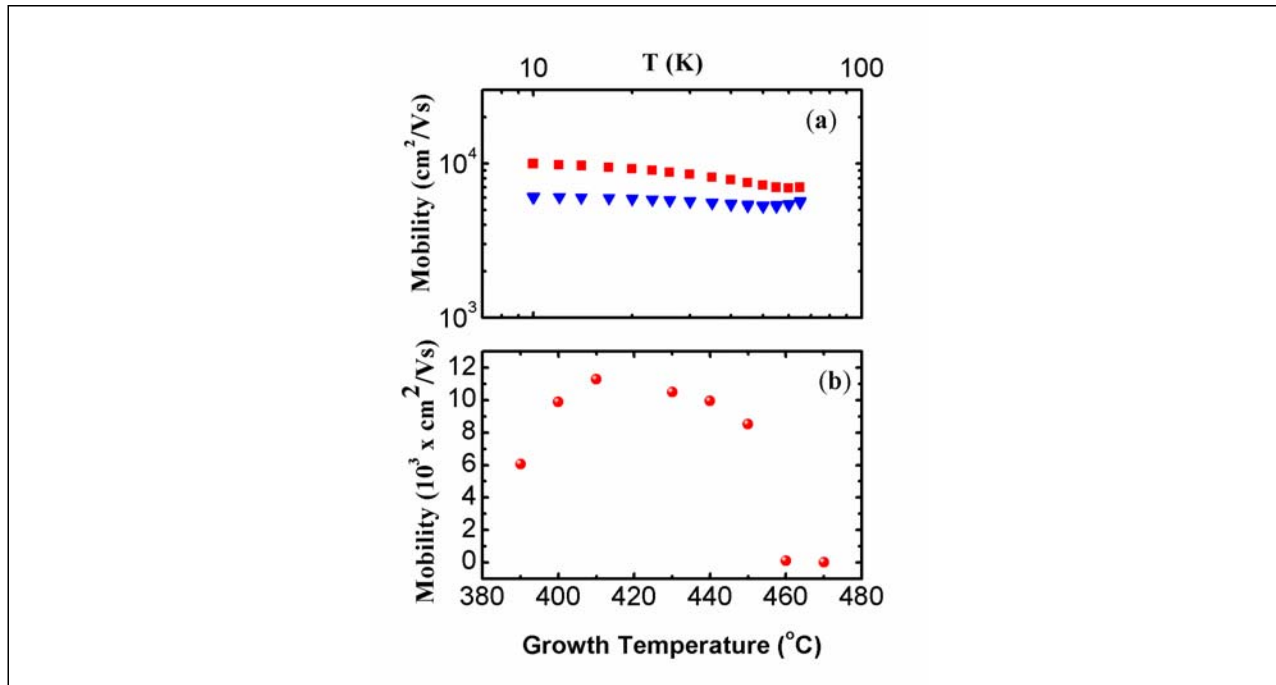

Figure 5. (a) Temperature dependence of the carrier mobility as a function of T for SL samples grown at 440 (red solid squares) and 390 °C (blue solid triangles). (b) The mobility as a function of growth temperature.

To measure the minority carrier lifetime, we performed time-resolved differential reflectivity measurements at 300 K on a SL sample. The pump was the output of an optical parametric amplifier (OPA), which was pumped by a regeneratively amplified Ti:Sapphire laser (CPA-2001, Clark-MXR, Inc.) with a repetition rate of 1 kHz. The wavelength of the OPA beam was tuned to 1.5 µm. The probe was the output of a continuous wave (CW) laser diode with a wavelength of 780 nm. A silicon balanced detector with a bandwidth of 350 MHz (PDB130A, Thorlabs, Inc.) was used to measure the difference in optical power between a reference arm of the probe beam, and the probe beam reflected from the surface of the sample at the pump spot. By measuring the RF output of the balanced detector with a fast oscilloscope, we were able to measure the change in reflectivity due to the pump with a time resolution of ~1 ns. Figure 6 shows the result of this measurement at 300 K. We interpret that the change in differential reflectivity is caused by a change in the index of refraction due to the presence of optically excited carriers. Here, we see multiple exponential decay components in the differential reflectivity. After fitting the data with the sum of four exponentials, we determined that the dominant contribution of recombination lifetimes comes from an exponential with a decay time of ~70 ns. We note that the actual recombination lifetimes from the bulk SL layer are likely to be longer than the measured lifetimes demonstrated in here; since our sample was grown without carrier isolating barriers, carrier leakage out of the SL and subsequent surface and substrate recombination are expected to contribute to the measured recombination rate.

Distribution Statement A. Approved for public release; distribution unlimited.

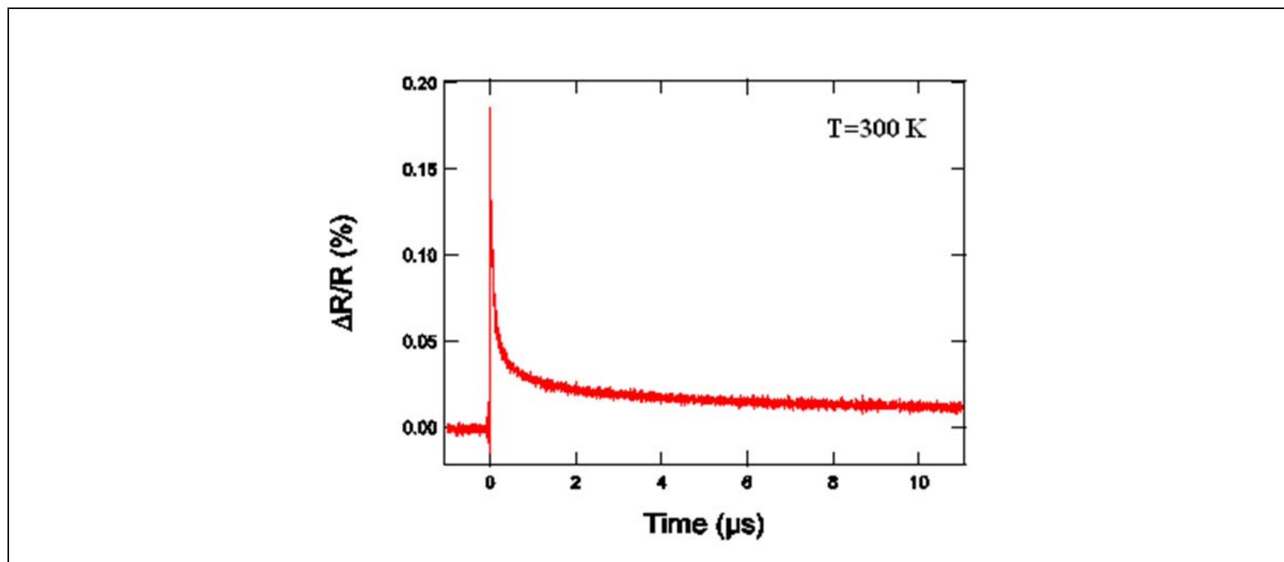

Figure 6. Time-resolved differential reflectivity data for a ~50 meV 47 Å InAs/21.5 Å $In_{0.25}GaSb_{0.75}$ superlattice sample at 300 K. The dominant recombination carrier lifetime was measured to be ~70 ns.

In conclusion, a combination of photoconductivity, temperature dependent Hall, and time-resolved differential reflectivity measurements was used to investigate the impact of T_g on the material quality of VLWIR InAs/GaInSb SLs. For the studies, a series of 47.0 Å InAs/21.5 Å $Ga_{0.75}In_{0.25}Sb$ SLs were grown by MBE at T_g ranging from 390 to 470 °C. The results showed that our MBE growth process used to create a ternary SL structure produced a consistent band gap of 50±5 meV. However the material quality of the grown samples assessed by PR intensity and Hall mobility was very sensitive to T_g. We observed a general trend of improving PR intensity as the temperature increases. The PR signal exhibited a maximum at 440 °C, and then dropped rapidly to less than 0.1 a. u. at higher temperatures. The SLs were all residual n-type, however the mobility varied between 11,300 and 21 cm^2/Vs. The mobility of the SL grown at 440 °C was approximately 10,000 V/cm^2 with a sheet carrier concentration of $5x10^{11}$ cm^{-2}, however the mobility precipitously dropped to 21 cm^2/Vs at higher temperatures. The 300 K recombination lifetime of an optimized SL sample that produced a strong PR signal was roughly 70 ns.

REFERENCES

1 D. L. Smith and C. Mailhiot, J. Appl. Phys. **62**, 2545 (1987).

2 C. H. Grein, W. H. Lau, T. L. Harbert, and M. E. Flatté, Proc. SPIE **4795**, 39 (2002).

3 C. H. Grein, J. Garland, and M. E. Flatté, J. Electron. Mat. **38**, 1800 (2009).

4 Y. Wei, A. Gin, M. Razeghi, and G. J. Brown, Appl. Phys. Lett. **80**, 3262 (2002).

5 H. Mohseni, Y. Wei, and M. Razeghi, Proc. SPIE **4288**, 191 (2001).

6 Y. Wei, A. Gin, M. Razeghi, and G. J. Brown, Appl. Phys. Lett. **81**, 3675 (2002).

7 H. Mohseni, M. Razeghi, G. J. Brown, and Y. S. Park, Appl. Phys. Lett. **78**, 2107 (2001).

Distribution Statement A. Approved for public release; distribution unlimited.

8 E. H. Aifer, E. M. Jackson, G. Boishin, L. J. Whitman, I. Vurgaftman, J. R. Meyer, J. C. Culbertson, and B. R. Bennett, Appl. Phys. Lett. **82**, 4411 (2003).

9 W. C. Mitchel, S. Elhamri, H. J. Haugan, and G. J. Brown, to be published.

10 K. Mahalingam, H. J. Haugan, G. J. Brown, K. G. Eyink, and Bin Jiang Proc. SPIE **8268**, 826831 (2012).

11 H. J. Haugan, G. J. Brown, S. Elhamri, S. Pacley, B. V. Olson, and T. F. Boggess, J. Appl. Phys. **111**, 053113 (2012)

2.3 Quantitative Analysis of Strain Distribution in $InAs/InAs_{(1-x)}Sb_x$ Superlattices

Krishnamurthy Mahalingam, Elizabeth H. Steenbergen, Gail J. Brown
AFRL/RXAN, Materials and Manufacturing Directorate, Air Force Research Laboratory, Wright Patterson AFB OH 45433-7707

Yong-Hang Zhang
School of Electrical, Computer and Energy Engineering, Arizona State University, Tempe, Arizona 85287, USA

Abstract
Atomic resolution transmission electron microscopy is performed to examine the strain distribution in an $InAs/InAs_{(1-x)}Sb_x$ superlattice, grown on a (100)-GaSb substrate. The strain profiles reveal that the thickness of tensile regions in the superlattice is significantly lower than expected, with a corresponding increase in thickness of the compressive regions. Furthermore, significant grading is observed within the tensile regions of the strain profile, indicating Sb intermixing from the InAsSb growth surface. The results signify an effective reduction in the InAs layer thickness due to the anion (As-Sb) exchange process at the InAs-on-InAsSb interface.

INTRODUCTION
Arsenide/antimonide based III-V semiconductor strained layer superlattices have attracted significant attention as tunable device materials for mid- to very long-wavelength infrared detection.[1-10] There are two categories of interest: those based on the $InAs/In_xGa_{(1-x)}Sb$ system, and others based on the Ga-free $InAs/InAs_xSb_{(1-x)}$ system. While $InAs/In_xGa_{(1-x)}Sb$ superlattices have been extensively studied for over two decades,[1-5] $InAs/InAs_xSb_{(1-x)}$ superlattices have only recently emerged as potential alternatives,[6-10] due to their superior minority carrier lifetime, which is attributed to the absence of Ga-induced SRH defects.[7-9] A critical aspect in the design and growth of these materials is balancing the superlattice strain, which needs to be performed such that, in addition to achieving high structural quality, the appropriate composition and associated strain of the constituent layers are maintained over the whole structure. Proper strain profiles across individual layers in the superlattice is particularly important for tailoring of the superlattice band structure and related properties.[4] An examination of the local strain distribution within the superlattice is then important, since it provides a direct means for investigating atomistic processes that control structural evolution during growth and for understanding how these affect key properties of the overall structure. Atomic scale strain distribution studies have been recently been reported on $InAs/In_xGa_{(1-x)}Sb$ superlattices, which revealed the nature of strain localization at interfaces and surface segregation within GaSb layers.[11,12] There is however a lack of similar studies on $InAs/InAs_xSb_{(1-x)}$ superlattices. The objective of the present

Distribution Statement A. Approved for public release; distribution unlimited.

communication is to apply recent advancements in high-resolution transmission electron microscopy (HRTEM) to examine the nature of strain distribution in InAs/ $InAs_{(1-x)}Sb_x$ superlattices. The approach employed is similar to that described in recent studies,[11] wherein aberration corrected HRTEM is used in combination with advanced digital image analysis to obtain strain maps across thin layers (1 – 2 nm) at high spatial resolution.

RESULTS AND DISCUSSION

The superlattice sample investigated in this study was grown on a (100) GaSb substrate by molecular beam epitaxy, having a nominal period of 7.2 nm, with nominal thickness values of 5.8 nm for InAs and 1.5 nm for $InAs_{(1-x)}Sb_x$, and a nominal value of x= 0.4 for the composition. Cross-sectional samples for TEM observations along the orthogonal [011] and [0-11] zone axes were prepared by conventional ion-milling, with the sample mounted on a liquid-nitrogen cooled cryo-stage. The HRTEM observations were performed using a Titan 80-300 TEM equipped with a spherical aberration (image) corrector. The constituent layers in the superlattice were examined using the negative spherical aberration (C_s) imaging (NCSI) method,[13,14] wherein the nominal value of C_s was set to -20 μm and the images acquired at over-focus settings in the range of 6-10 nm. Under these imaging conditions the projected atomic columns appear bright on a dark background, providing high contrast and enhanced spatial resolution of the cation and anion sublattices for precise location of the atomic columns and subsequent measurement of local lattice displacements (of the order of 10 picometers).[11,13,14]

Figure 7 is an X-ray diffraction profile of the (400) reflection from the sample. The superlattice is closely lattice matched to the GaSb substrate, which is evident from the small separation in the respective peak positions. The superlattice period as measured from the superlattice satellite peaks was 7.3 nm. Figure 8(a) is a dark-field TEM image obtained using the chemically sensitive (200) reflections, wherein the InAs and InAsSb layers appear bright and dark, respectively. Measurement of the individual layer thicknesses from these images, based on the delineation of image contrast, yielded an average value of 5.5 ± 0.14 nm for the InAs layers and 1.8 ± 0.1 nm for InAsSb layers. The distinct dark contrast typically seen at interfaces in (200) - dark field images of InAs/InGaSb superlattices[15] is not observed in these structures. A profile of the intensity distribution across the layers in the superlattice, shown in Figure 8(b), indicates a grading in the composition in the interfacial regions.

Distribution Statement A. Approved for public release; distribution unlimited.

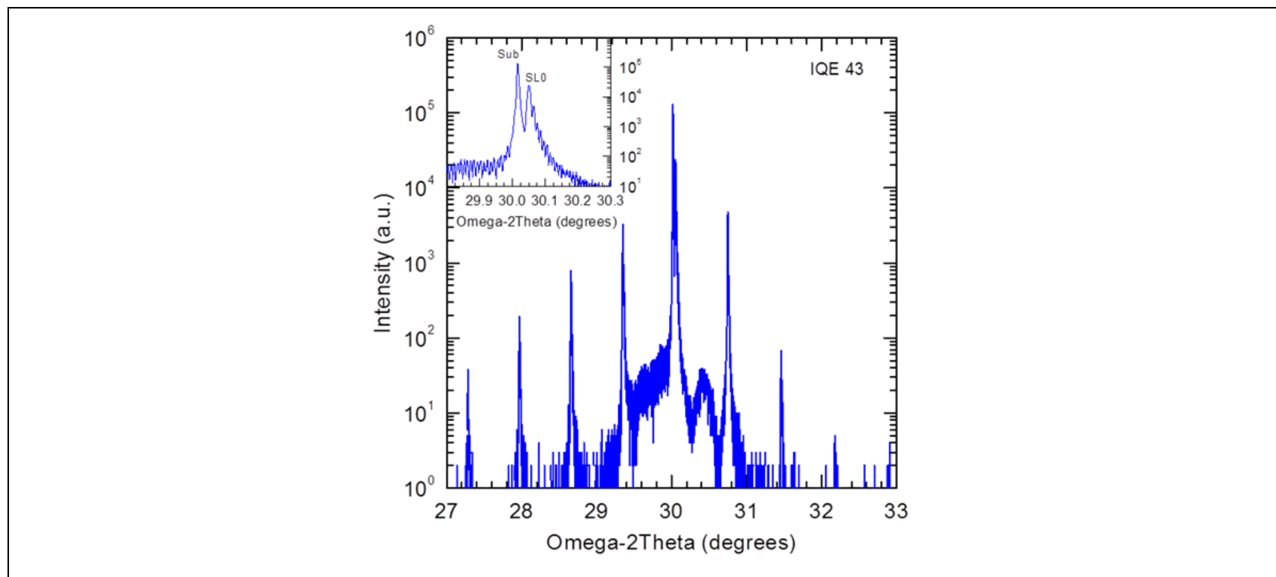

Figure 7. (400) ω-2θ X-ray diffraction scan of the InAs/InAsSb SL with the inset showing the substrate peak and the SL zero-order peak.

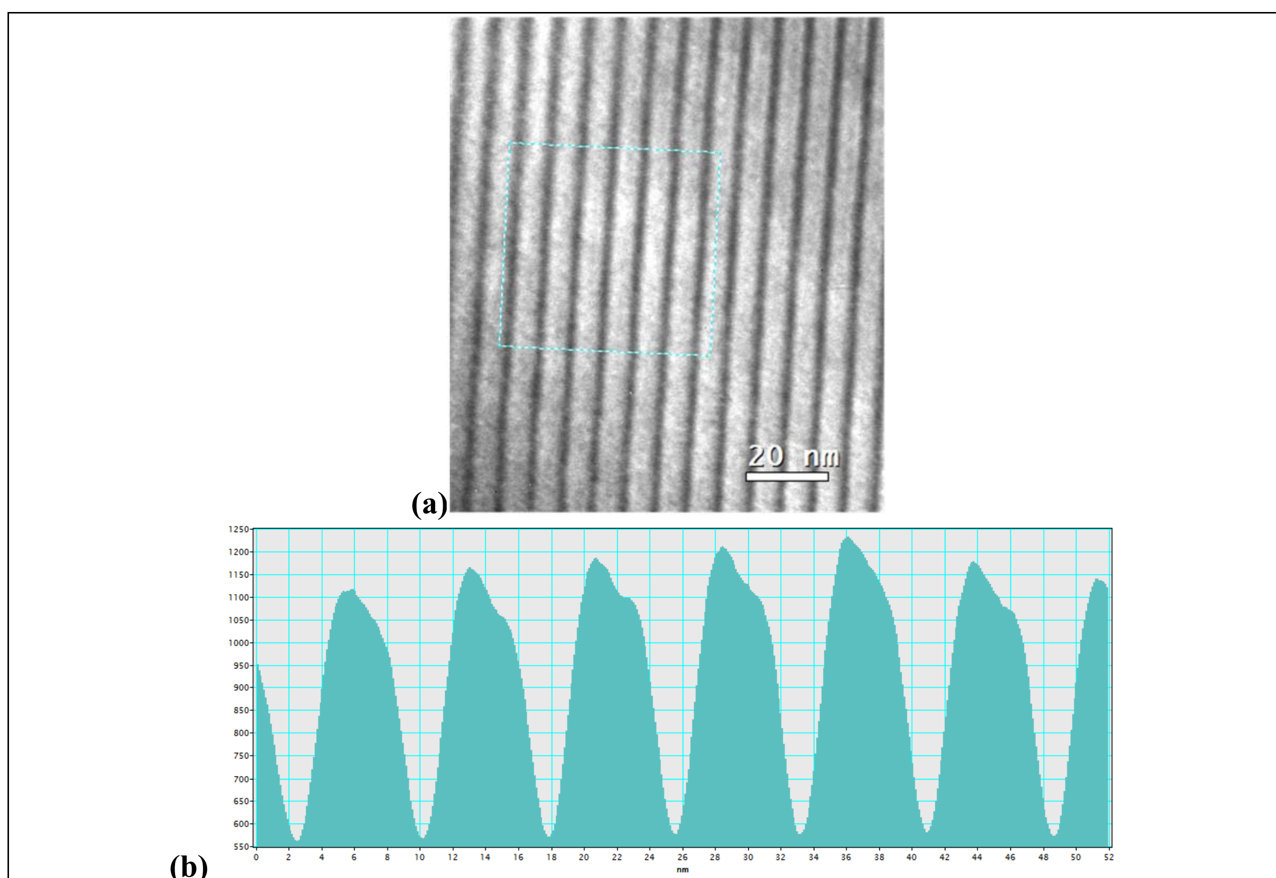

Figure 8. (a) (200) dark-field image of the superlattice, showing the InAs (bright) and the $InAs_xSb_{(1-x)}$ (dark), and (b) the intensity profile within the marked region in (a), average parallel to the interfaces, showing grading in the InAs layers.

Distribution Statement A. Approved for public release; distribution unlimited.

Figure 9 is an HRTEM image of the superlattice structure (after applying a background subtraction filter[16] for noise removal) showing the first few layers above the substrate, wherein the bright dots in this image correspond to the projected atomic columns. To obtain the strain distribution in the superlattice, these images were further analyzed by the peak-pair method,[17] using a commercial software package (HREM Research, Inc.). The procedure adopted was similar to that described in the original publication by Galindo et al.,[17] except that the Bragg filtering step was excluded, in order to retain all spatial frequency components contributing to the image. The analysis was performed such that the strain component ε_{xx} was parallel to the interface (along [011]) and ε_{yy} was along the growth direction ([100]). The two components were determined with respect to an averaged reference lattice in the substrate (GaSb) region.

Figure 9 A high-resolution TEM image of the superlattice where the bright dots correspond to the projected atomic columns.

Similar to previous studies, a detailed analysis of the maps of the two components showed that the values for ε_{xx} are negligible, thereby indicating that the interfaces are coherent.[11] Figures 10 (a) and (b) show the map of the strain component ε_{yy} and its profile over a region including the first few periods of the superlattice adjacent to the substrate. The strain map in Figure 10 (a) clearly delineates the compressive (yellow/red) and tensile (green/blue) regions in the superlattice, corresponding to the InAsSb and InAs layers, respectively. From the strain profile shown in Figure 10 (b), the mean value of the peak strain in the InAsSb layers was measured to be 0.023, yielding a value of x = 0.25 for $InAs_{(1-x)}Sb_x$. The average superlattice period determined from peak-to-peak separation in the strain profile was 7.3 nm, in good agreement with those measured by X-ray diffraction profile and dark-field imaging. However, a measurement of the thickness of individual layers in the strain map indicated a significantly lower value of 4.66 ± 0.13 nm for the region in tensile strain and a corresponding higher value of 2.62 ± 0.05 nm for regions in compressive strain. The strain profiles thus indicate an effective reduction of over 15% in the InAs layer thickness.

Distribution Statement A. Approved for public release; distribution unlimited.

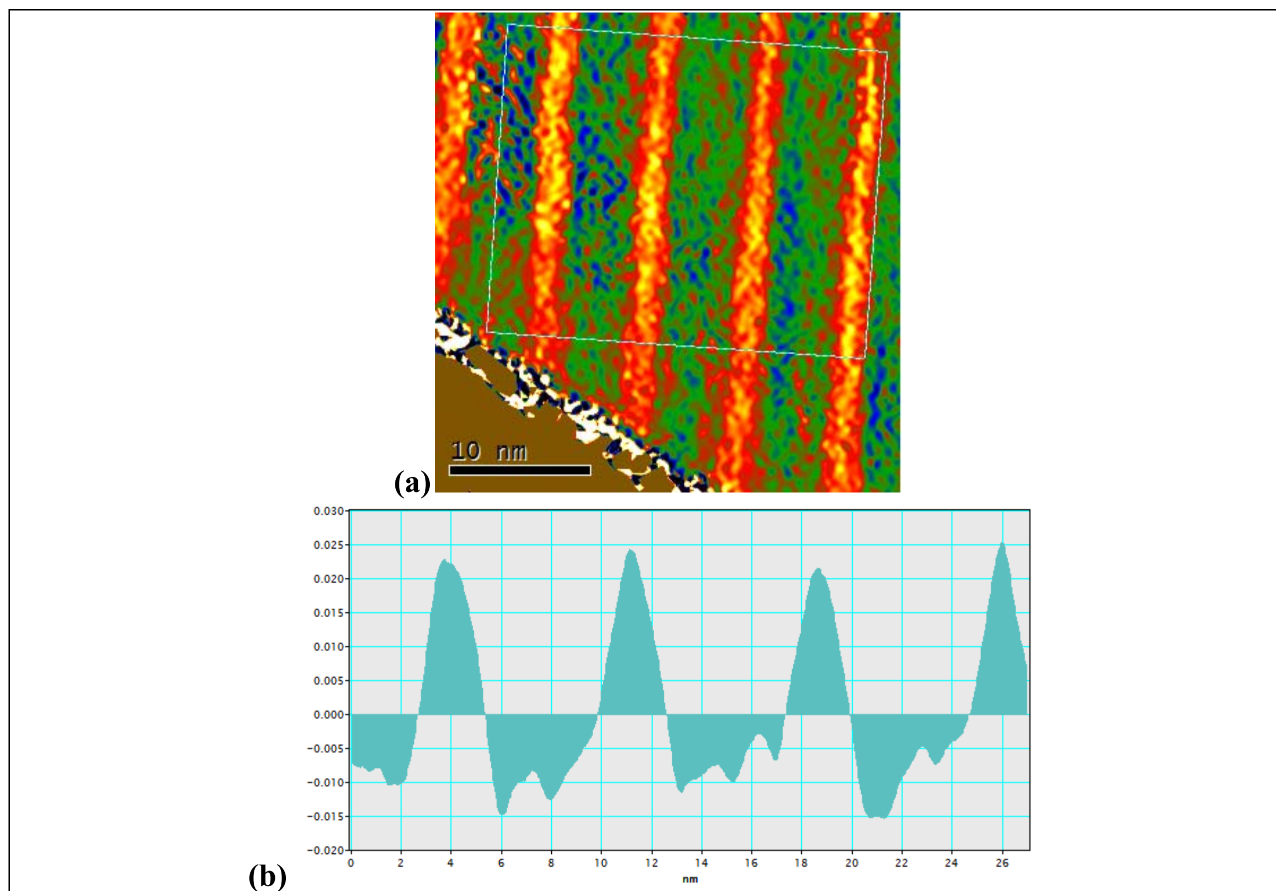

Figure 10. (a) A strain map of the strain tensor ε_{yy}, along the growth direction, and (b) a plot of the strain profile, averaged parallel to the interface, within the marked region in (a).

To further examine the strain distribution within each layer in the superlattice, the mean strain profile was obtained from aligning by cross-correlation and averaging over the three periods in the boxed region in Figure 10 (a). The resulting profile, shown in Figure 11, clearly reveals an asymmetric grading in the InAs layer, with a slow increase in the tensile strain at the InAs-on-InAsSb interface (right) and a relatively abrupt change from tensile to compressive strain at the InAsSb-on-InAs interface (left). The grading in the strain profile observed in the vicinity of the InAs-on-InAsSb interface indicates an incorporation of Sb into InAs, most likely due to surface segregation of Sb from the InAsSb layer, induced by the As-Sb exchange reaction.[18,19] As additional support to the observed strained profile, a comparison of the intensity profile in Figure 8(b) was performed by inverting the image in Figure 8(a) and rescaling the pixel values to the same range as that for the strain map in Figure 10(a). Figure 11 shows the average intensity profile for the (inverted) (200) dark-field image, obtained from a similar averaging procedure as that for the strain profile. A direct correlation between the two profiles is evident and, given the compositional sensitivity of the zinc-blende (200) reflection,[20] clearly indicates a grading in chemical composition.

Distribution Statement A. Approved for public release; distribution unlimited.

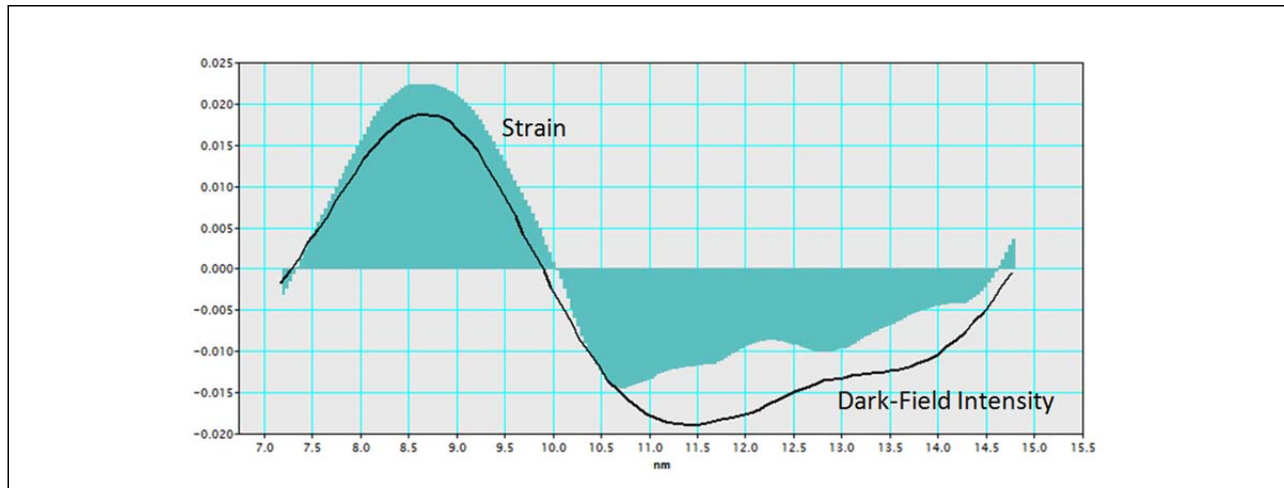

Figure 11. (a) Profile of the strain tensor ε_{yy} (shaded) and the (200) dark-field intensity (black line) averaged over three superlattice periods.

It is of interest to compare the above results with those reported in similar studies on $InAs/In_xGa_{(1-x)}Sb$ superlattices.[11,12] It is well known that strain localization at interfaces and the need to tailor interface composition plays an important role in Ga-based superlattices, due to the formation of Ga-As (tensile) and In-Sb (compressive) bonds at the interface. In the present study, however, the need for interface composition control is alleviated due to the absence of Ga in these superlattices. Indeed, a comparison of the strain profile in Figure 10, with those reported for $InAs-In_xGa_{(1-x)}Sb$,[11,12] show that the strong negative spikes due to the dominant presence of Ga-As bonds (in interfaces with no composition control), are not observed herein. The present results however indicate that anion segregation at the InAs-on-InAsSb interface must be addressed, which should be possible by appropriate control of As/Sb and V/III flux ratios.[19]

In summary, the strain distribution across interfaces in an $InAs/InAs_{(1-x)}Sb_x$ superlattice was investigated by aberration corrected HRTEM. The strain profiles (ε_{yy}) revealed significant reduction in the InAs layer thickness and also compositional grading within these layers, due to the segregation of Sb from the InAsSb surface. To preserve the designed InAs layer thickness and composition, the As-Sb exchange reaction at the InAs-on-InAsSb interface must be controlled, which is important since the band gap of the superlattice and related properties are sensitive to monolayer fluctuations in its thickness.[21]

REFERENCES

1. D. R. Rhiger, J. Electron. Mat. **40**, 1815 (2011).
2. A. Rogalski, J. Antoszewski, and L. Faraone J. Appl. Phys. **105**, 091101 (2009)
3. G. J. Brown, Proceedings of SPIE **5783**, 457 (2005).
4. D. L. Smith and C. Mailhiot, J. Appl. Phys. **62**, 2545(1987).
5. G. A. Sai-Halasz, R. Tsu and L. Esaki, Appl. Phys. Lett. **30**, 651 (1977).
6. D. Lackner, O. J. Pitts, M. Steger, A. Yang, M. L. W. Thewalt, and S. P. Watkins, Appl. Phys. Lett. **95**, 081906 (2009)

Distribution Statement A. Approved for public release; distribution unlimited.

7. E. H. Steenbergen, B. C. Connelly, G. D. Metcalfe, H. Shen, M. Wraback, D. Lubyshev, Y. Qiu, J. M. Fastenau, A. W. K. Liu, S. Elhamri, O. O. Cellek, and Y.-H. Zhang, Appl. Phys. Lett. **99**, 251110 (2011).

8. H. S. Kim, O. O. Cellek, Zhi-Yuan Lin, Zhao-Yu He, Xin-Hao Zhao, Shi Liu, H. Li, and Y.-H. Zhang, Appl. Phys. Lett. 101, 161114 (2012).

9. B. V. Olson, E. A. Shaner, J. K. Kim, J. F. Klem, S. D. Hawkins, L. M. Murray, J. P. Prineas, M. E. Flatté, and T. F. Boggess, Appl. Phys. Lett. **101**, 092109 (2012).

10. T. Schuler-Sandy, S. Myers, B. Klein, N. Gautam, P. Ahirwar, Z.-B. Tian, T. Rotter, G. Balakrishnan, E. Plis, and S. Krishna, Appl. Phys. Lett. **101**, 071111 (2012).

11. K. Mahalingam, H. J. Haugan, G. J. Brown and K. G. Eyink, Ultramicroscopy **127**, 70 (2013)

12. H. J. Haugan, G. J. Brown, S. Elhamri, W. C. Mitchel, K. Mahalingam, M. Kim, G. T. Noe, N. E. Ogden, and J. Kono, Appl. Phys. Lett. **101**, 171105 (2012)

13. C. L. Jia, M. Lentzen and K. Urban, Science **299**, 870 (2003) .

14. C. L. Jia, L. Houben, A. Thust and J. Barthel, Ultramicroscopy **110**, 500 (2010).

15. K. Mahalingam, K. G. Eyink, G. J. Brown, D. L. Dorsey, C. F. Kisielowski, and A. Thust, J. Microscopy **230**, 372 (2008).

16. R. Kilaas, J. Microscopy **55**, 45 (1998).

17. P. L.Galindo, S.Kret, A. M. Sanchez, J-Y. Laval, A. Yanez, J. Pizarro, E. Guerrero, T. Ben, and S. I. Molina, Ultramicroscopy **107**, 1186 (2007).

18. J. Steinshnider, J. Harper, M. Weimer, C. -H. Lin, and S. S. Pei, Phys. Rev. Lett. **85**, 4562 (2000), and references therein.

19. G. J. Sullivan, A. Ikhlassi, J. Bergman, R. E. DeWames, J.R. Waldrop, C. Grein, M. Flatté, K. Mahalingam, H. Yang, M. Zhong and M. Weimer, J. Vac. Sci. Tech. **B23**, 1144 (2005).

20. E. G. Bithell, E. G. and W. M. Stobbs, Philos. Mag. **60**, 39 (1989).

21. H. J. Haugan, L. Grazulis, G. J. Brown, K. Mahalingam, D. H. Tomich, J. Cryst. Growth **261**, 471 (2004).

2.4 Post Growth Annealing Study on LWIR InAs/GaSb Superlattices

H. J. Haugan,[1, a)] G. J. Brown,[1] S. Elhamri,[2] S. Pacley,[1] B. V. Olson,[3] and T. F. Boggess[3]
[1]Air Force Research Laboratory, Materials & Manufacturing Directorate, Wright-Patterson Air Force Base, Ohio 45433, USA
[2]Department of Physics, University of Dayton, Ohio 45469, USA
[3]Department of Physics and Astronomy, University of Iowa, Iowa City, Iowa 52242, USA

ABSTRACT
The impact of post growth annealing on the electrical properties of a long wavelength infrared type-II superlattice (SL) was explored. Quarters of a single SL wafer were annealed at 440, 480 and 515 °C respectively for 30 minutes. Changes in the electrical properties were followed using spectral photoconductivity, temperature dependent Hall effect and time-resolved pump-probe

Distribution Statement A. Approved for public release; distribution unlimited.

measurements. The band gap energy remained at ~107 meV for each anneal and the photoresponse spectra showed a 25% improvement. The carrier lifetime increased from 12 ns to ~15 ns with annealing. While the electron mobility showed little change for the 440 and 480 °C anneals, it increased from ~4500 cm^2/Vs to 6300 cm^2/Vs for the 515 °C anneal.

INTRODUCTION

There has been a steady effort in developing long wavelength infrared (LWIR) photodetectors using InAs/GaSb superlattice (SL) materials due to their capability for engineering the band structure to optimize detector performance. For instance, by creating a larger energy separation between the heavy-hole and light-hole bands than the SL energy band gap, Auger recombination rates can be substantially reduced. Grein *et al.*[1] reported that for the LWIR band, an ideal SL would have substantial performance enhancement due to the suppression of Auger recombination processes. Unfortunately, most reported epitaxially grown InAs/GaSb superlattices exhibit overall carrier lifetimes less than 100 nanoseconds (ns).[2, 3] Due to the large number of Shockley-Read-Hall (SRH) defects generated during the deposition process, SL photodiodes cannot be operated at theoretically predicted performance levels. Unless significant improvements are made to resolve intrinsic defect issues in these SL materials, the defect-related generation-recombination process in SL photodiodes will still be the dominant cause of short minority carrier lifetime. In the past years, we have explored a variety of growth parameters to reduce defects and background carriers in the mid-wavelength infrared (MWIR) InAs/GaSb SL materials.[4-7] However, our studies show that the epitaxial growth parameters optimized for MWIR SL growth are not directly applicable for LWIR SL growth.

In this study, a combination of spectral photoconductivity, temperature dependent Hall effect, and time-resolved pump-probe studies on a controlled set of SL samples was used to explore LWIR SL material optimization. The impact of post growth annealing on the charge carrier density, mobility, photoresponse (PR) intensity and recombination dynamics is reported in the following sections.

RESULTS AND DISCUSSION

In order to assess the impact of post growth annealing on the lifetime limiting defects and electrical properties, a sample set containing one unannealed control and three annealed quarters of the same two inch diameter epitaxial wafer were studied. The SL stack and buffer layer were deposited on a lightly doped n-type GaSb (100) wafer, which provides a high enough resistivity substrate for electrical measurements. The 0.3 μm thick GaSb buffer layer was grown at 490 °C followed by growth of a 0.5 μm thick SL stack at 400 °C. The 0.5 μm thick SL stack was composed of 16 MLs InAs/7 MLs GaSb with a band gap energy of 107 meV and a photoresponse onset at 11.6 μm. The V/III beam equivalent flux ratio was around 3-4 for both InAs and GaSb layers, with growth rates of 0.4-0.6 Å/s for the InAs layers and 0.6 Å/s for the GaSb layers. The intended SL structure was confirmed by high resolution X-ray rocking curves. The measured period of the control sample was 68 Å.

After the SL growth, the last layer was terminated with a arsenic (As) capping layer to protect the SL during ex-situ cleaving of the wafer into quarters. Of these 4 samples, one went back into the growth chamber to remove the As-cap layer and was kept as a control sample (unannealed). Another quarter went back into the growth chamber to remove the As-cap layer and then

Distribution Statement A. Approved for public release; distribution unlimited.

immediately annealed in-situ at 440 ±10 °C for 30 minutes under a Sb-over pressure of $6x10^{-7}$ torr. The same procedure was used for the other two quarters with in-situ annealing temperatures of 480 °C and 515°C respectively. Samples for Hall effect, spectral photoconductivity and carrier lifetime were cut from each of these quarters.

For the carrier lifetime measurements, the four samples were analyzed by a pump-probe technique. Direct measurement of minority carrier lifetimes in LWIR SLs has recently been conducted by time-resolved photoluminescence.[8] Here we present time-resolved differential transmission measurements[9] using an electronically delayed pump-probe technique.[10] A commercially available amplified, titanium: sapphire laser was used to pump an optical parametric amplifier where, through difference frequency generation, pump pulses of 250 fs duration and a wavelength of 4.6 µm were generated and used to excite electron-hole pairs in the SLs. The long wavelength of the pump pulse ensures that the optically injected carriers are injected uniformly through the SL and not in the GaSb substrate or cap. A 9.3 µm quantum cascade laser, with a full width at half maximum pulse duration of 3 ns, was used to probe near the band gap of the SLs, and was synchronized with the 1 kHz pump by a precision electronic delay generator. By electronically scanning the time delay between the pump and probe, recombination processes that occur on time scales ranging from a few nanoseconds to a millisecond can be measured. The pump and probe were focused to radii (e^{-2} of the intensity) of 715 and 290 µm, respectively and spatially overlapped on the sample, which was held at 77 K inside a closed-loop Helium cooled cryostat. The pump was chopped at 500 Hz and the transmitted probe was detected by a single-element HgCdTe detector cooled to 77 K. A long-pass filter was placed before the detector to eliminate pump scatter. The pump-induced change in probe transmission was extracted from the detector signal using a "gate and hold" method consisting of two gated integrator and lock-in amplifier pairs, one pair measured ΔT and the other the transmission of the probe in the absence of a pump pulse. The differential transmission was recorded as a function of temporal delay between the pump and probe and pump pulse energy, which was varied from 80 to 20 nJ. The SL absorption coefficient at 4.6 µm was calculated to be 1600 cm^{-1}, corresponding to 8 % of the pump being absorbed in the SL. To exclude any $\Delta T/T$ signature arising from the substrate, measurements were made on similar LWIR SL material with the substrate removed and it was found that the observed $\Delta T/T$ is exclusive to the SLs.

The time-resolved $\Delta T/T$ data were well described by a simple model incorporating the cross-correlation between a Gaussian probe pulse and a mono-exponential decay. The carrier recombination rates were extracted from these fits. On the relatively long time scales and large optically excited area considered here, the excited carrier population is assumed to be uniform throughout the probed portion of SL and to have been instantaneously generated by the ultrafast pump pulse. The differential transmission for our control sample is shown in Figure 1a for several excess carrier densities, the lowest of which corresponds to an average carrier density of 2×10^{16} cm^{-3}. The inset to Figure 1a shows that, in the range of carrier densities probed, the peak $\Delta T/T$ has a linear dependence on excess carrier density. Hence, the temporal evolution of $\Delta T/T$ directly reflects the temporal evolution of the optically injected carrier density. Figure 1b shows the recombination rate vs. excess carrier density for both control and annealed SL samples. The recombination rates show a linear dependence on carrier density indicating that Auger processes are negligible at these densities and that the minority carrier lifetime can be extracted as the

Distribution Statement A. Approved for public release; distribution unlimited.

inverse of the y-intercept.[3] Using this method, minority carrier lifetimes of 12.0 and 15.4 ns were measured for the control and 440 °C annealed SL samples, respectively. Lifetimes for the other two samples are listed in Table 2 and show no additional improvement at the higher anneals. As these samples were grown without carrier confinement barriers, carrier leakage out of the SL and the subsequent surface and substrate recombination are expected to contribute to the measured minority carrier lifetimes. The measured decay rate is, therefore, an upper limit to the SRH recombination rate. That is, the actual SRH lifetimes from the SL are likely longer than the measured lifetimes. We note that, in addition to the somewhat longer lifetime in the annealed samples, the data in Figure 12b show that this sample has a greater radiative decay component, as indicated by the somewhat larger slope. Both the longer measured lifetime and the larger radiative decay component are consistent with the modest improvement in the quality of the annealed SL sample.

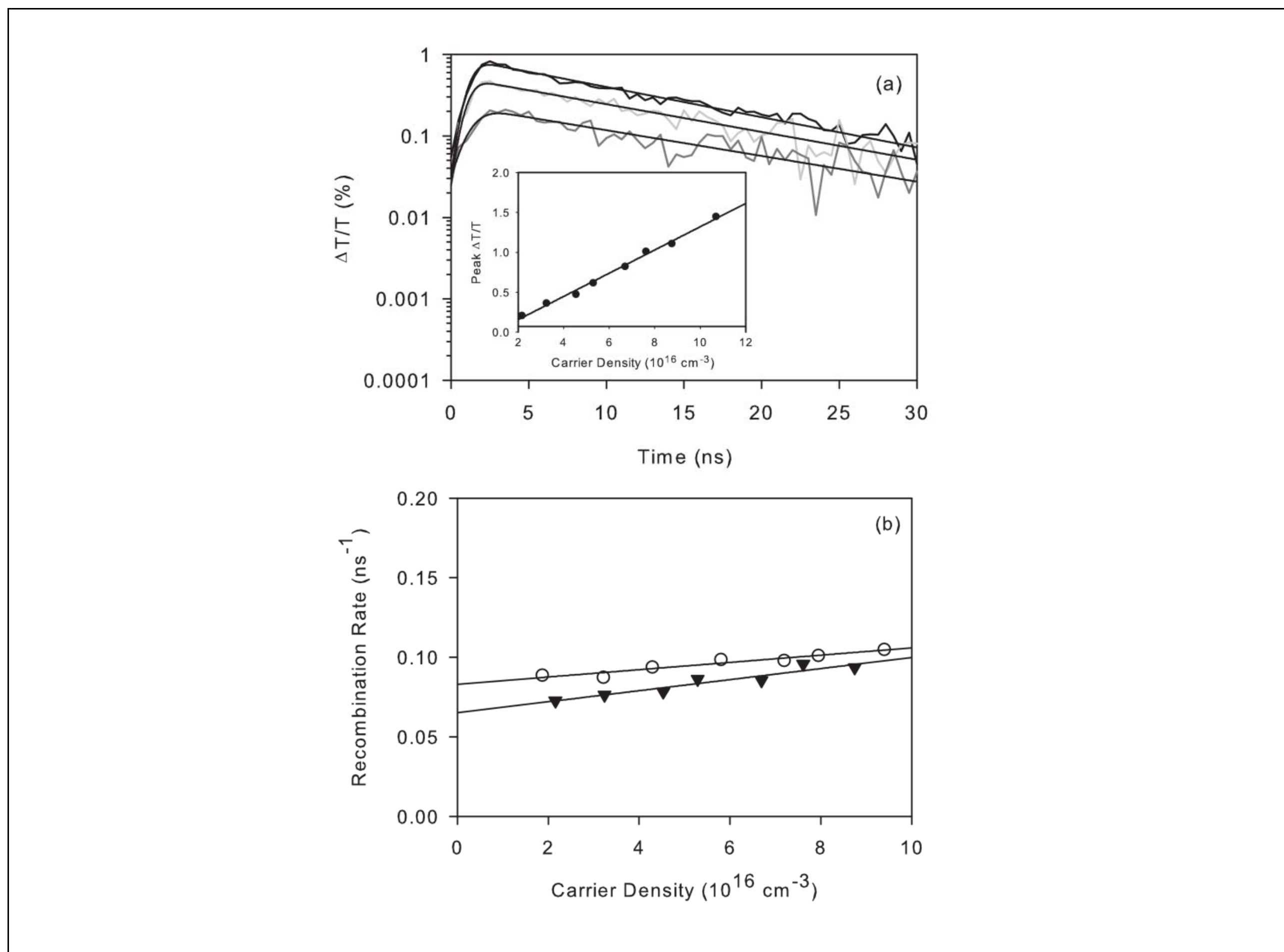

Figure 12. (a) The time-resolved differential transmission decays with model fits for a control 0.5 µm thick 16 MLs InAs/7 MLs GaSb SL sample. The pump fluence ranges from 3-0.6 µJ/cm^2. The lowest curve corresponds to an average excess carrier density of 2 x 10^{16} cm^{-3}. The inset shows the linear dependence of the peak ΔT/T on the excess carrier density. (b) The inverse lifetime vs. excess carrier density for the control (open circles) and annealed SL samples (solid triangles). The minority carrier lifetimes were measured to be 12.0 ns and 15.4 ns for the control and annealed SL samples, respectively and were found as the y-intercept of a linear fit to the data.

Distribution Statement A. Approved for public release; distribution unlimited.

Table 2. Summary of the measurement results for the sample set. The photoresponse and Hall results are from measurements at 10K. The cut-off wavelength (λ_c) is selected at the point where the intensity drops by 50%. The PR intensity was measured at 85 meV above the band gap. All of the samples were n-type.

sample	Anneal (°C)	E_g (meV)	λ_c (μm)	PR Intensity (arb. units)	Sheet carrier (cm^{-2})	Mobility ($cm^2/V s$)	Lifetime (ns)
A	control	107.2	10.3	5.1	1.59 E+12	4800	12
B	440	107.8	10.2	3.7	1.89 E+12	4258	15.4
C	480	109.2	10.2	6.5	2.03 E+12	4005	14.6
D	515	109.4	10.3	6.2	1.13 E+12	6336	15.2

The impact of annealing on the SL sheet carrier density and mobility was investigated using variable temperature resistivity and Hall effect measurements. The variation of the carrier density and the in-plane mobility for each SL along with those of the GaSb substrate are shown in Figure 13. The higher resistivity GaSb substrate enabled isolation of the superlattice charge carriers from those of the substrate at temperatures up to 80K. Hall measurements on the GaSb substrate were performed on a pristine wafer from the same lot as the wafer used for the SL growth. The carrier density curves are tightly grouped at temperatures below 25K. The carrier densities at 10K are listed in Table 2 along with the corresponding mobilities. The mobility curves are very similar between the samples, with three of the samples having mobilities in the range of 4000 to 4800 cm^2/Vs at low temperature. The SL annealed at 515 °C has a higher mobility over a wide temperature range and is relatively temperature independent up to 80K. The higher mobility (6300 cm2/Vs) and nature of the T dependence indicate that the interface roughness may be reduced slightly with the 515 °C anneal.

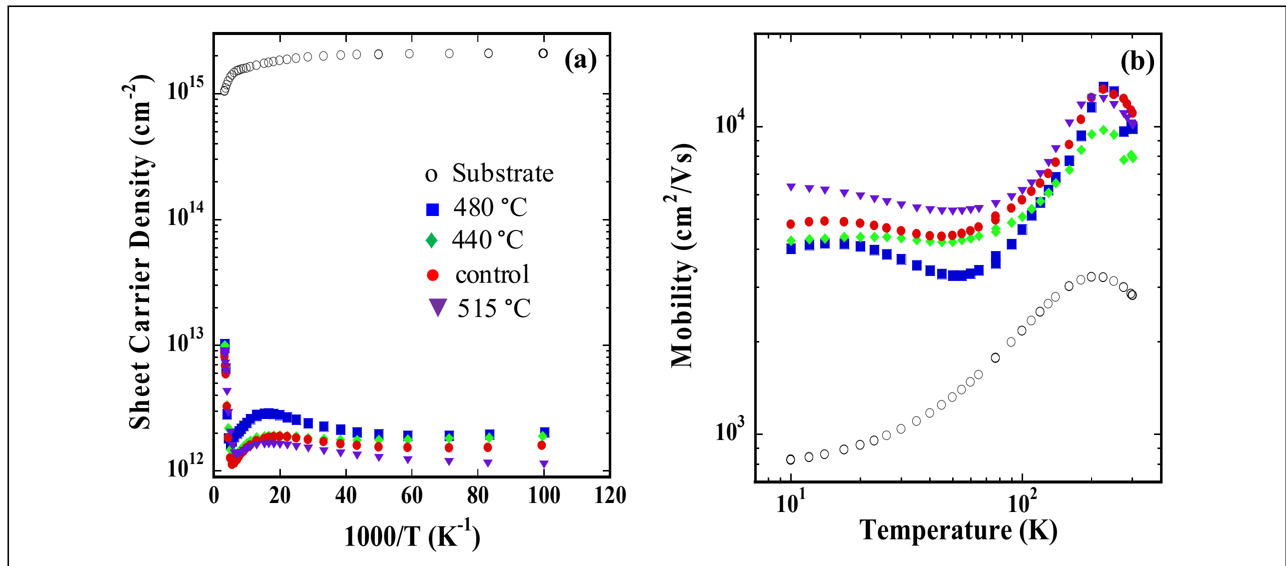

Figure 13. Temperature dependence of (a) the sheet carrier density as a function of 1000/T, and (b) the carrier mobility as a function of T of the unannealed and three annealed SL samples. The measurements on a lightly doped n-type GaSb substrate are included to demonstrate the insignificant impact of the substrate on the SL parameters at low T.

Distribution Statement A. Approved for public release; distribution unlimited.

Since the strength of photoresponse signal is a strong function of the overall material quality, PR spectra were used to identify the spectral range of the material and strength of the optically excited signal. The spectra were collected with a Fourier Transform Infrared spectrometer at a temperature of 10 K. Due to the relatively low resistivity of the samples, the photoconductivity was measured in the current biased mode, with a current of 0.5 mA between two parallel strip contacts on the surface. Figure 14 shows the four PR spectra collected from the sample set. Although the PR intensities are given in arbitrary units, the relative signal strengths can still be compared as the test conditions for all the samples were kept constant. The band gap energies reported in Table 2 were determined by fitting a straight line along the band edge transition and noting the intersection with the energy axis. Since the band gap energy remained fairly constant, showing a shift of less than 2 meV, it can be concluded that the SL layers are not interdiffusing and that samples taken from all four quarters are very consistent. Similar to the carrier lifetime results, the photoresponse is modestly enhanced (~25% increase in signal) by the annealing. The typical error in PR intensity from test to test is about 10% which means the slight decrease in photoresponse at 515 °C is not significant. The result of a lower PR intensity for the 440 °C anneal is unexpected but does follow the slightly lower mobility and higher carrier density measured. Previous studies on other SL designs had found annealing at ≥450 °C to be beneficial which agrees with the PR, Hall and lifetime results.[11,12]

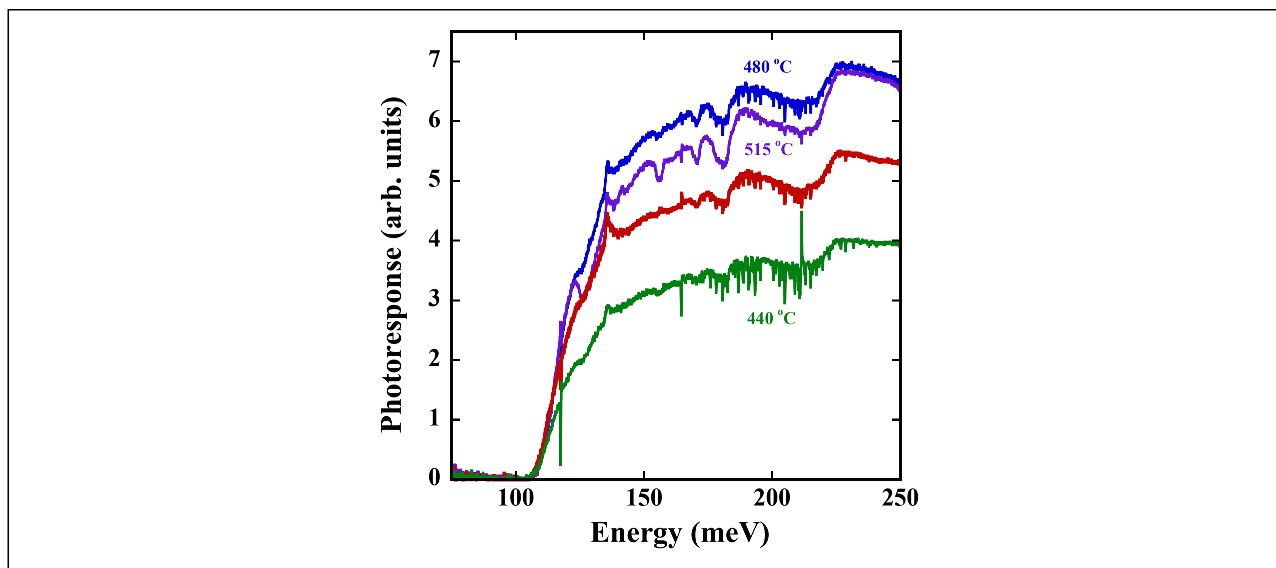

Figure 14. Comparison of the photoresponse spectra from the control and three annealed SL samples measured at 10K. The annealing temperatures for each sample producing the spectrum are indicated. The small features on the spectra come from water vapor, organic residues and 60 Hz noise spikes.

CONCLUSIONS

A combination of photoconductivity, temperature dependent Hall, and time-resolved differential transmission measurements, which used an electronically delayed pump-probe technique, was used to investigate the benefits of post growth, in-situ annealing on a LWIR InAs/GaSb superlattice. The carrier lifetime showed some improvement with annealing, increasing from 12 to 15.4 ns. The electron mobilities were relatively unaffected with the exception of the 515 °C anneal results where the carrier concentration decreased and the mobility jumped from ~4500

Distribution Statement A. Approved for public release; distribution unlimited.

cm^2/Vs to 6300 cm^2/Vs. The photoresponse spectra showed a 25% improvement in signal for the 480 °C and 515 °C anneals. Overall the LWIR SLs benefit from a higher post growth anneal than found in earlier studies where 450 °C was the optimum.

REFERENCES

1 C. H. Grein, J. Garland, and M. E. Flatté, J. Electron. Mat. **38**, 1800 (2009).

2 J. Pellegrino and R. DeWames, Proc. SPIE **7298**, 72981U (2009).

3 D. Donetsky, G. Belenky, S. Svensson, and S. Suchalkin, Appl. Phys. Lett. **97**, 051208 (2010).

4 H. J. Haugan, G. J. Brown, and L. Grazulis, J. Vac. Sci. Technol. **B 29**, 03C101 (2011).

5 H. J. Haugan, S. Elhamri, F. Szmulowicz, B. Ullrich, G. J. Brown, and W. C. Mitchel, Appl. Phys. Lett. **92**, 071102 (2008).

6 H. J. Haugan, B. Ullrich, S. Elhamri, F. Szmulowicz, G. J. Brown, L. C. Tung, and Y. J. Wang, J. Appl. Phys. **107**, 083112 (2010).

7 H. J. Haugan, B. Ullrich, L. Grazulis, S. Elhamri, G. J. Brown, and W. C. Mitchel, J. Vac. Sci. Technol. **B 28**, C3C19 (2010).

8 B. C. Connelly, G. D. Metcalfe, H. Shen, and M. Wraback, Appl. Phys. Lett. **97**, 25117 (2010).

9 S. W. McCahon, S. A. Anson, D.-J. Jang, M. E. Flatté, T. F. Boggess, D. H. Chow, T. C. Hasenberg, and C. H. Grein, Appl. Phys. Lett. **68**, 2135 (1996).

10 U. Schmidhammer, S. Roth, E. Riedle, A. A. Tishkov, and H. Mayr, Rev. Sci. Instrum. **76**, 093111 (2005).

11 H. J. Haugan, S. Elhamri, G. J. Brown, and W. C. Mitchel, J. Appl. Phys. **104**, 073111 (2008).

12 C.-H. Lin, A. Anselm, C.-H. Kuo, A. Delaney, G. J. Brown, K. Mahalingam, A. W. Saxler, R. J. Linville and F. Szmulowicz, Proc. SPIE **3948**, 133 (2000).

2.5 Strain analysis of compositionally tailored interfaces in InAs/GaSb superlattices

Krishnamurthy Mahalingam, Heather J. Haugan, and Gail J. Brown
Air Force Research Laboratory, Materials and Manufacturing Directorate, Wright Patterson AFB, OH 45433-7707

Abstract

The effect of interface composition control on interfacial strain distribution in InAs/GaSb superlattices on (100)-GaSb substrates is investigated by atomic resolution scanning transmission electron microscopy. The interface composition was controlled by either depositing InSb at each interface, or soaking the GaSb-on-InAs interface under Sb_2 atmosphere. The strain profiles reveal a distinct difference in the extent to which the superlattice strain is balanced using the two methods. In particular, they indicate that the degree of strain balance achievable with soaking is inherently limited by arsenic surface coverage during GaSb-on-InAs interface formation, emphasizing the influence of V/III flux ratio at this interface. The results also explain observed X-ray diffraction profiles.

Distribution Statement A. Approved for public release; distribution unlimited.

INTRODUCTION

InAs/GaSb superlattices display interesting optical and electronic properties[1] that are well suited for many device applications, such as infrared detectors [2-4] and lasers. [5-7] Matching the effective lattice constant of the superlattice to its substrate, also referred to as strain balancing, is critical, and is performed by precise control of interface composition during growth.[8] It is well known that the local strain at interfaces can be significant due to the fact that both cations and anions change across each interface, resulting in interfacial bonds of the type : Ga-As and In-Sb.[8,9] The interfacial strain is then dependent on the prevalent bond type, being tensile for Ga-As bonds and compressive for In-Sb bonds. Recent X-ray diffraction studies have shown that subtle change in the interface composition causes substantial change in the overall superlattice strain, as measured from the separation of the superlattice and substrate peaks.[8] Detailed studies on the composition profiles of such interfaces have been reported.[11-12] However, for a fundamental insight into how local changes in interface composition relate to the overall superlattice strain determined by X-ray diffraction, a direct examination of the local strain at interfaces is highly desirable. In this report we have performed such a study, wherein quantitative analysis of the strain distribution across compositionally controlled interfaces in InAs/GaS superlattices is investigated by aberration corrected scanning transmission electron microscopy (STEM), using the high-angle annular dark-field (HAADF) imaging technique.[13] The enhanced spatial resolution at the atomic scale realized by aberration correction, combined with the high contrast due to atomic number sensitivity in HAADF technique enables direct imaging of the cation and anion sublattices. Furthermore, digital analysis of these images using peak pair analysis (PPA),[14] permits precise measurement of local atomic displacements, from which a map of the strain distribution in the superlattice is determined with respect to an averaged reference lattice in the substrate region.

RESULTS AND DISCUSSION

The superlattices investigated in this study were grown on (100) GaSb substrates by molecular beam epitaxy, using conditions described in detail in a previous report.[8] The nominal superlattice period was 7.0 nm, with intended thickness of 4.9 nm for InAs layers and 2.1 nm for GaSb layers. The samples examined consisted of superlattices in which the interfaces were formed under with no composition control, and those in which the interfaces were formed with controlled modification of chemical composition. Two types of interfacial composition control were investigated: structures wherein each interface was tailored to be "InSb-like," by a controlled deposition of 0.8 ML of InSb after completion of each GaSb or InAs layer and structures where a growth interruption (soaking) of 6 sec under an Sb_2 flux was performed only at the InAs growth surface, prior to deposition of the GaSb layer. Cross-sectional samples, for imaging along the [011] and [0 $\bar{1}$ 1] zone axes, were prepared by liquid N_2 cooled ion-milling. The observations were performed using the TEAM 0.5 transmission electron microscope (NCEM, Berkeley, CA), operated at 300 kV.

Figure 15 shows the X-ray diffraction profile of the (400) reflection from the three samples, where the well-defined pendellosung fringes around the superlattice peak indicate high structural quality of the constituent layers. A systematic change in the separation between the substrate and superlattice peak is observed, showing that interface composition control has a significant effect on the overall superlattice strain. The superlattice with no interface control is in tensile strain with respect to the GaSb substrate, whereas that with the InSb deposition is nearly strain balanced. The superlattice with soaking is in intermediate tensile strain.

Distribution Statement A. Approved for public release; distribution unlimited.

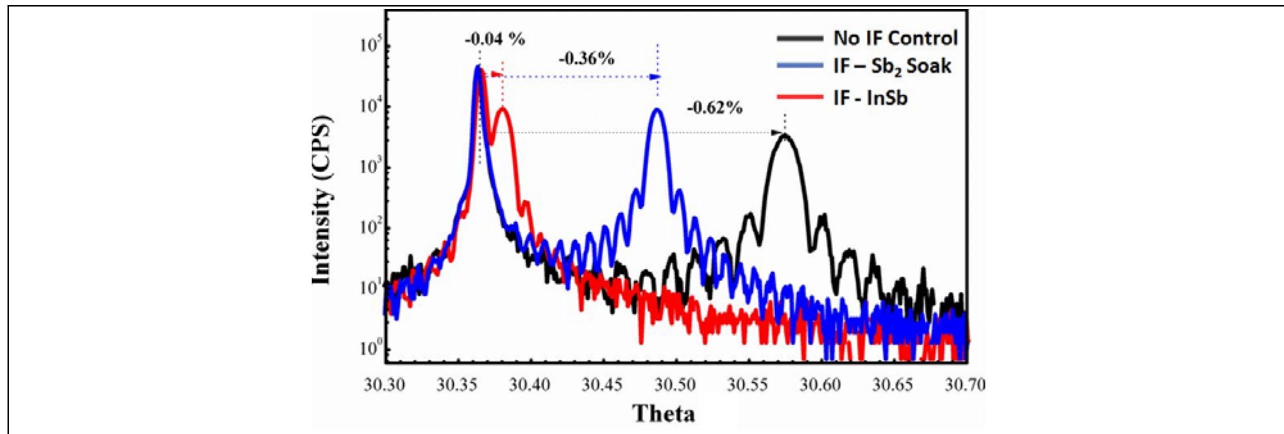

Figure 15. X-ray diffraction profiles of the (400) reflection showing the GaSb substrate and the superlattice peaks.

Figure 16 is a representative HAADF-STEM image of the different superlattices examined in this study, where the individual layers adjacent to the substrate are labeled and the position of interfaces identified by arrows (the background subtraction filter was applied for noise removal[15]). The bright dots in this image correspond to the projected atomic columns. The inset in Figure 16(a) is a magnified image of an interfacial region showing that the projected cation and anion columns are well separated to perform quantitative analysis of the lattice displacements. To quantify the strain distribution in superlattice these images were analyzed using the PPA method, as described in earlier reports. [9,14] The mapping procedure was performed such that the strain components ε_{xx} was parallel to the interface (along [011]) and ε_{yy} along the growth direction ([100]). Similar to the previous study [9] the profiles of ε_{xx} were negligible indicating that the interfaces are coherent with substrate, and that relaxation due TEM to sample preparation is insignificant.

Distribution Statement A. Approved for public release; distribution unlimited.

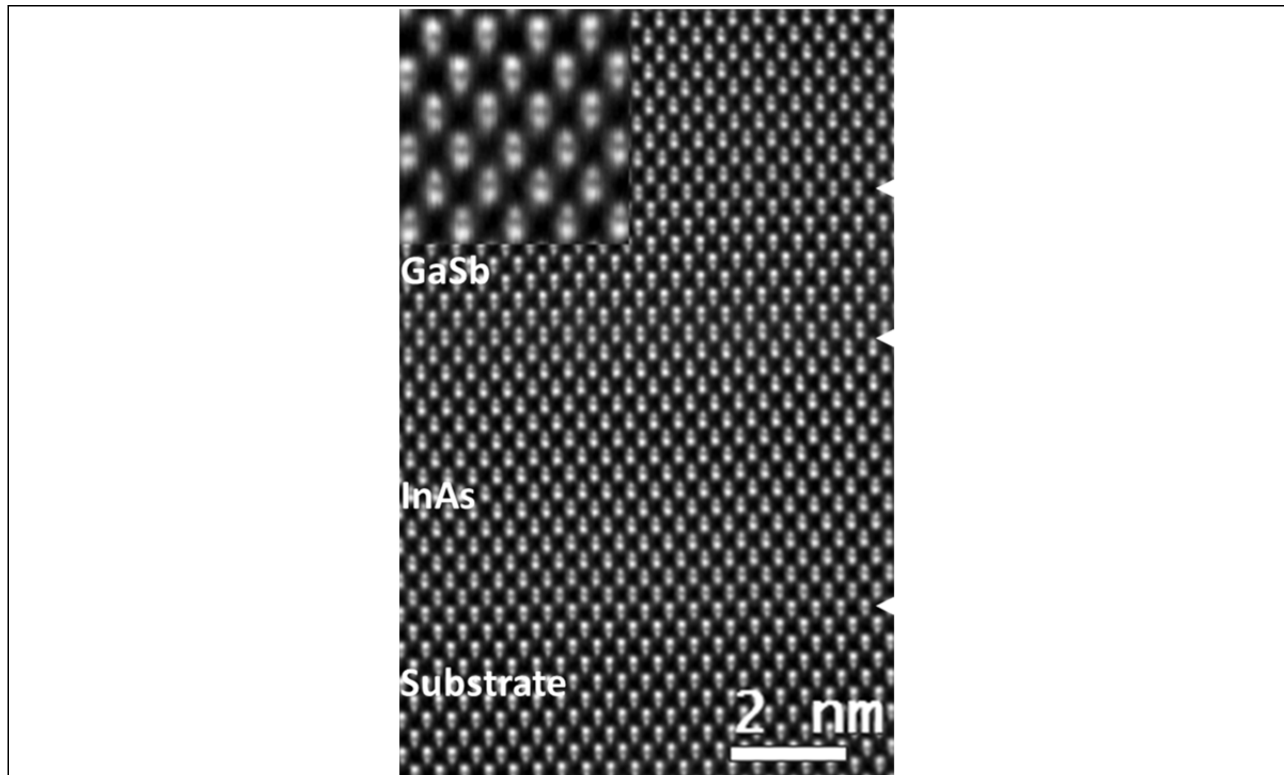

Figure 16. (a) HAADF-STEM image of the InAs/GaSb superlattice structure, where the arrows indicate position of interfaces. The inset on left is a magnified view of an interface showing well-resolved atomic columns .

Figure 17 (a) shows the map of the strain tensor, $\varepsilon_{yy,}$ for the superlattice grown with no interface control, where the compressive and tensile regions in the superlattice corresponding to the GaSb and InAs layers are clearly revealed. Figure 17(b) shows the strain profile, averaged along the interface. It is observed that the profile at each GaSb-on-InAs interface exhibits a prominent negative spike, indicating that this interface is in tensile strain and that the dominant bond type at this interface is Ga-As. The InAs-on-GaSb interfaces exhibit strain inversion so that the effective strain in these regions is negligible. Also, the thin GaSb layers within the superlattice are consistently compressively strained, indicating incorporation of In into these layers which. Based on the GaAs-like nature of the GaSb-on-InAs interface, this can be due to surface segregation of In caused by the In-Ga exchange process during deposition of GaSb on InAs.[10]

Distribution Statement A. Approved for public release; distribution unlimited.

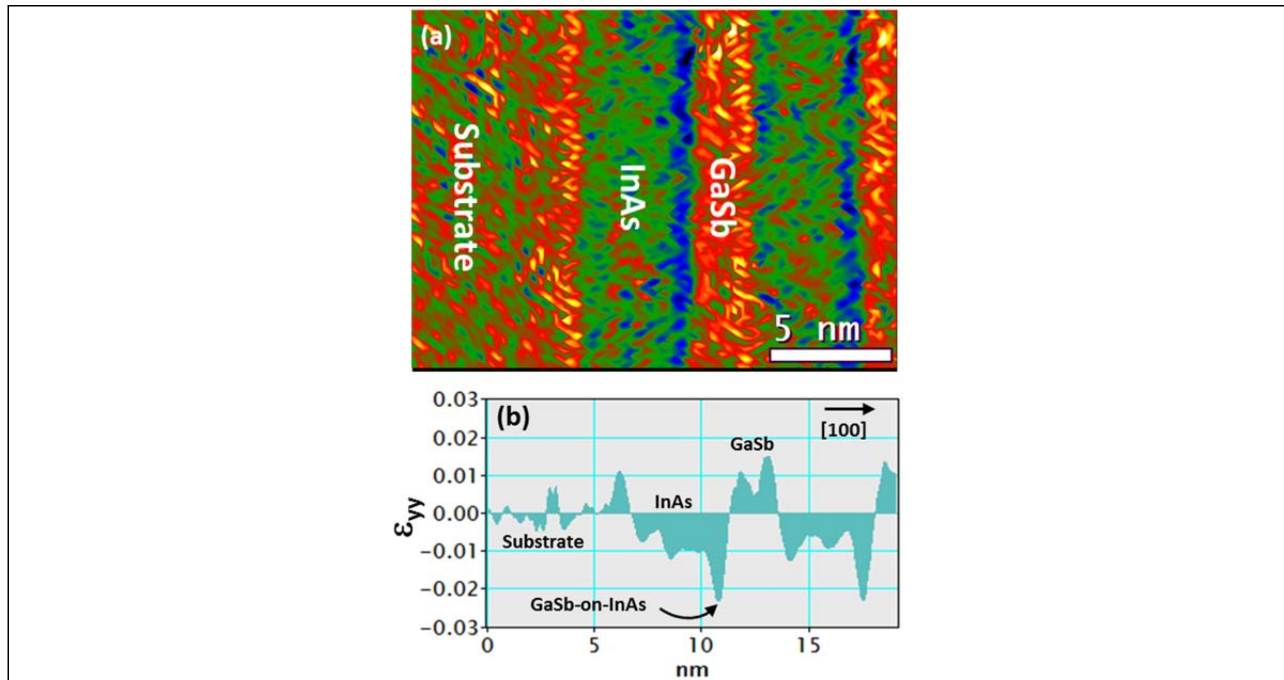

Figure 17. Strain analysis of the superlattice with no interface control showing (a) the map of the strain tensor, ε_{yy} and (b) a plot of the strain profile averaged parallel to the interface over the whole image in (a).

Figure 18 (a) shows the strain map for the superlattice grown with InSb deposition at each interface along with the averaged strain profile in Figure 18 (b). A comparison with the profiles in Figure 17 (b) shows that the negative spikes at the GaSb-on-InAs interface are not present. A sharply peaked compressive strain is observed at both interfaces (indicated by arrows), which is consistent with shift in the superlattice peak in the X-ray profiles (Figure 15).

Distribution Statement A. Approved for public release; distribution unlimited.

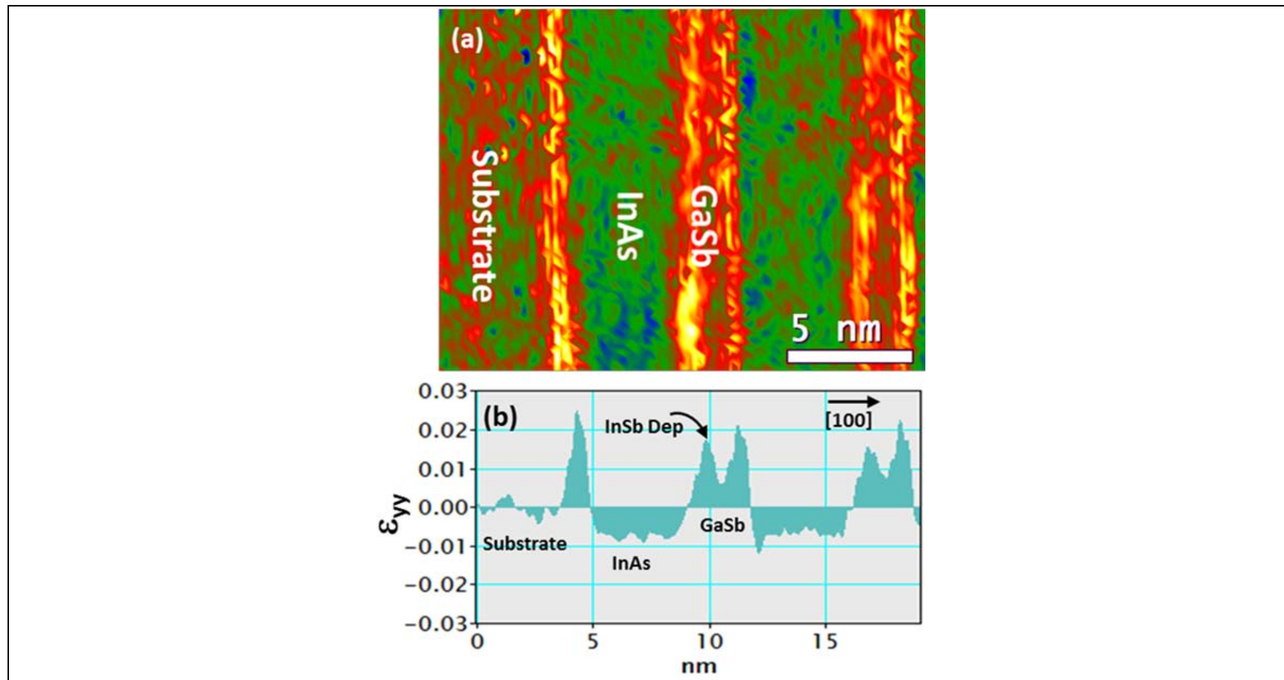

Figure 18. Strain analysis of the superlattice with InSb deposition showing (a) the map of the strain tensor, ε_{yy} and (b) a plot of the strain profile averaged parallel to the interface over the whole image in (a).

The strain map and the averaged strain profile for the superlattices grown with growth interruption at the GaSb-on-InAs interface is shown in Figs. 5 (a) and (b). Similar to the results shown in Figure 18, it is observed that the strain state changes from tensile to distinctly compressive at this interface. However, an analysis of images obtained from the orthogonal [011] zone axis, shown in Figs. 6 (a) and (b), reveals different results. Here it is clear that the GaSb-on-InAs interface is in tensile strain similar to that observed in superlattices with no interface control (as in Figure 17). These results indicate that the Sb_2 soaking only partially compensates the tensile strain at the GaSb-on-InAs interfaces, which also accounts for the intermediate tensile strain in the corresponding X-ray diffraction profile (Figure 15).

Distribution Statement A. Approved for public release; distribution unlimited.

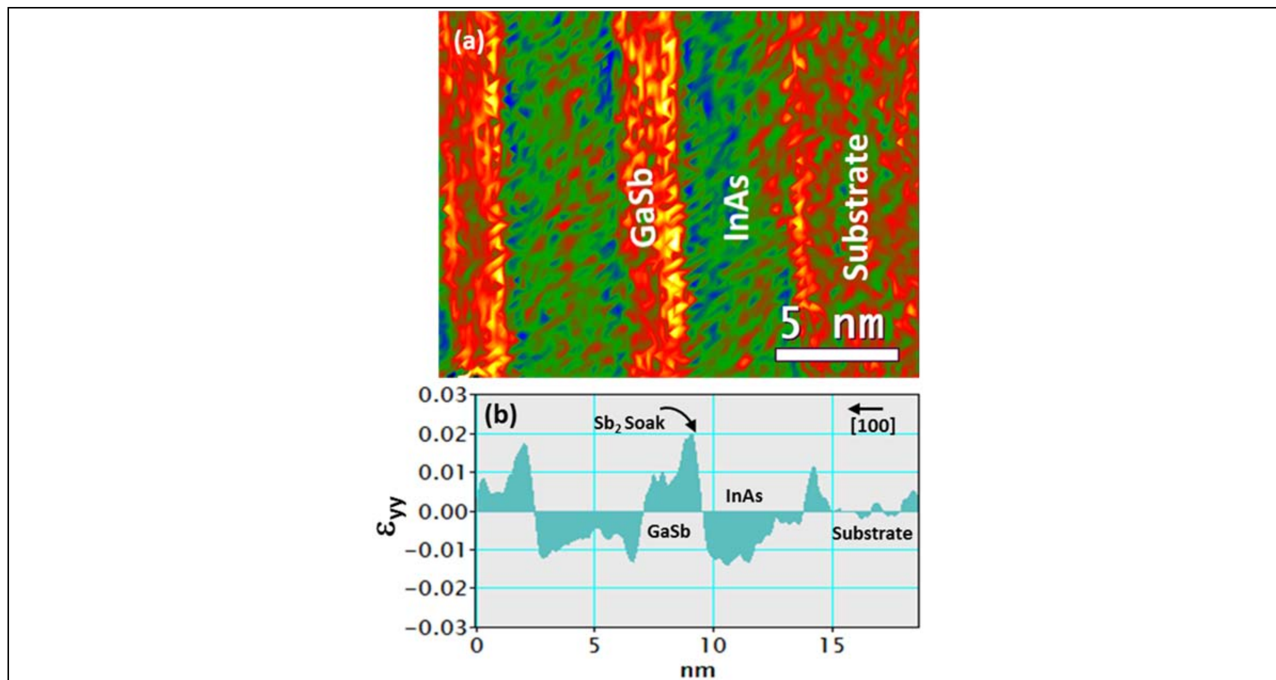

Figure 19. Strain analysis of the superlattice with Sb_2 soaking showing (a) the map of the strain tensor, ε_{yy} and (b) a plot of the strain profile averaged parallel to the interface over the whole image in (a). The analysis was performed on HAADF-STEM images acquired with the interfaces viewed along [011].

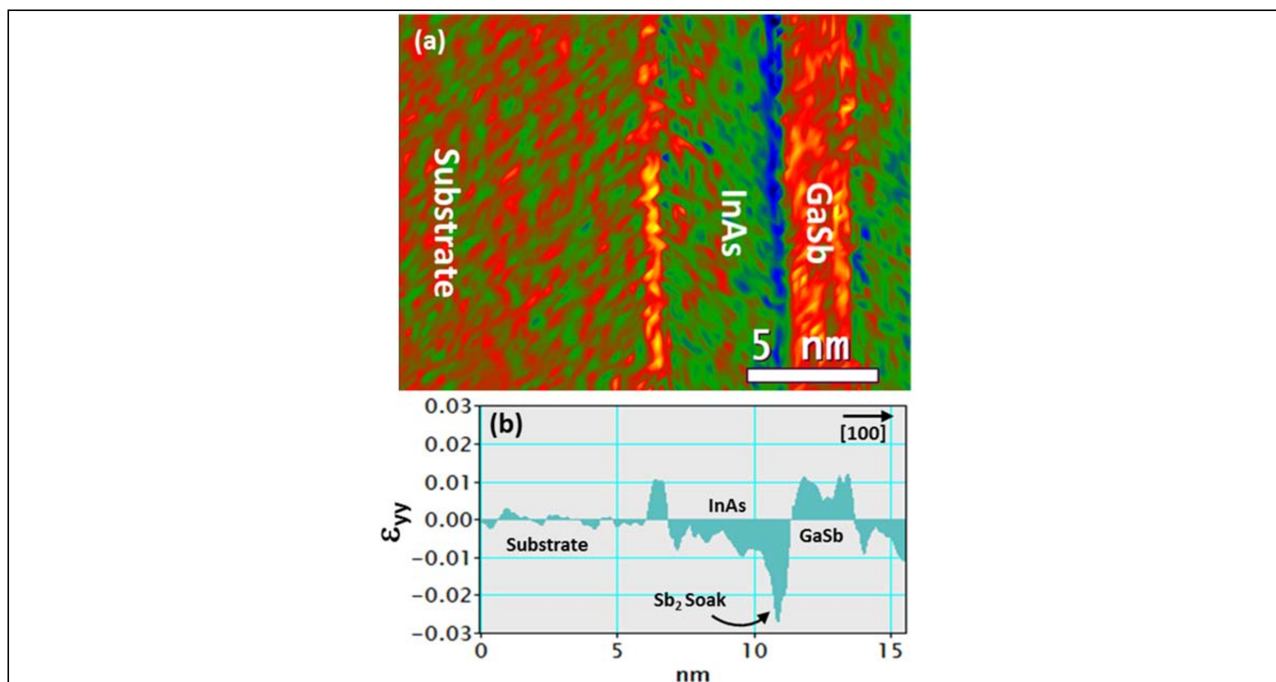

Figure 20. Strain analysis of the superlattice with Sb_2 soaking showing (a) the map of the strain tensor, ε_{yy} and (b) a plot of the strain profile averaged parallel to the interface over the whole image in (a). The analysis was performed on HAADF-STEM images acquired with the interfaces viewed along $[0\,\bar{1}\,1]$.

Distribution Statement A. Approved for public release; distribution unlimited.

It is worth reiterating that the different characteristics at the GaSb-on-InAs along orthogonal the two <011> was observed only in superlattices with soaking. In superlattices with no interface control and with InSb deposition, the strain at the GaSb-on-InAs interfaces in both cross-sections were similar to those presented in Figs. 3 and 4, respectively. These result can be explained by taking into consideration the polarity of the orthogonal <011> cross sections, where the two surface bonds on the group-III species are along [011] and those on the group-V species along [0 $\bar{1}$ 1].[16] In aberration-corrected HAADF-STEM imaging the polarity of the cross-section is easily determined by inspecting the Ga and Sb atomic columns in the substrate region. An examination of the GaSb region in the cross-sections of the samples with growth interruption, revealed that the orientation in Figure 19 was along [011] and that in Figure 20 along [0 $\bar{1}$ 1].

An explanation of the above results is proposed based on the consideration that under typical MBE growth conditions, the anion/cation surface coverage is strongly influenced by the V/III flux ratio. The propensity for Ga-As bond formation during deposition of GaSb at the InAs growth front (i.e. formation of the GaSb-on-InAs interface) is then dictated by the relative As/In surface coverage, where the surface-As contribution occurs by direct bonding from impinging Ga atoms and the surface-In contribution occurs from displacement due to the Ga-In exchange process (In surface segregation) . Under pre-deposition of 0.8 ML InSb, which is performed by first depositing In followed by exposure to Sb_2, it is clear that the resulting interface is compressive ("InSb-like") since the deposition of In restricts the surface-As coverage and the subsequent exposure to Sb_2 restricts the surface-exposed In. On the other hand, soaking under Sb_2 alone affects only the surface-In coverage, having little impact on the surface-As coverage (which is based on the fact that while the exchange of impinging As with bonded Sb is favored, the converse is not[17]). The Ga-As bonding resulting from this As-coverage is best revealed along the [0 $\bar{1}$ 1] zone-axis (Figure 20b) in the strain mapping procedure adopted herein, since it projects normal to the substrate and thus directly contributes to the strain tensor ε_{yy}, along the growth direction.

SUMMARY

In summary the strain mapping technique by HAADF-STEM reveals the impact of different methods used for interface composition control on the local strain profiles across interfaces, providing insight how they relate to the effective superlattice strain determined by X-ray diffraction. However, full distinction between strain profiles associated with the different techniques was possible only when orthogonal <011> cross-sections were examined. These measurements are important for optimizing growth conditions since the overall superlattice strain, and associated requirements for precisely tailoring interface composition, depend very much on the superlattice design.[18]

REFERENCES

1. G. A. Sai-Halasz, R. Tsu and L. Esaki, Appl. Phys. Lett. **30**, 651 (1977).
2. D. R. Rhiger, J. Electron. Mat. **40**, 1815 (2011).
3. G. J. Brown, Proceedings of SPIE **5783**, 457 (2005).
4. D. L. Smith and C. Mailhiot, J. Appl. Phys. **62**, 2545(1987).

Distribution Statement A. Approved for public release; distribution unlimited.

5. N. Deguffroy, V. Tasco, A. Gasseng, L. Cerutti, A. Trampert, A. N. Baranov and E. Tournie, Electron. Lett. **43**, 1285 (2007).
6. S. Ben Rejeb, M. Debbichi, M. Said, A.Gasseng, E. Tournie and P. Christol, J. Appl. Phys. **108**, 093107 (2010).
7. J. R. Meyer, C. A. Hoffman, F. J. Bartoli, and L. R. Ram-Mohan, *Appl. Phys. Lett.* **67**, 757 (1995).
8. H. J. Haugan, G. J. Brown, and L. Grazulis, J. Vac. Sci. Tech. **B29**, 03C101(2011).
9. K. Mahalingam, H. J. Haugan, G. J. Brown, and K. G. Eyink, Ultramicroscopy **127**, 70 (2013).
10. J. Steinshnider, J. Harper, M. Weimer, C. -H. Lin, and S. S. Pei, Phys. Rev. Lett. **85**, 4562 (2000), and references therein.
11. K. Mahalingam, K. G.Eyink, G. J. Brown, D. L.Dorsey, C. F. Kisielowski, and A. Thust, J. Microscopy **230**, 372-381 (2008).
12. H. Kim, Y. Meng, J. L. Rouviére, D. Isheim, D. N. Seidman, and J. M. Zuo, J. Appl. Phys. **113**, 103511 (2013).
13. S. J. Pennycook, and P. D. Nellist, *Scanning Transmission Electron Microscopy – Imaging and Analysis* (Springer, New York, 2011).
14. P. L.Galindo, S.Kret, A. M. Sanchez, J-Y. Laval, A. Yanez, J. Pizarro, E. Guerrero, T. Ben, and S. I. Molina, Ultramicroscopy **107**, 1186 (2007).
15. R. Kilaas, J. Microscopy **55**, 45-51(1998).
16. A. Y. Cho, J. App. Phys.***47***, 2841 (1976).
17. R. Kaspi, J. Steinshnider, M. Weimer, C. Moeller, A. Ongstad, J. Cryst. Growth **225**, 544 (2001).
18. H. J. Haugan, B. Ullrich, S. Elhamri, F. Szmulowicz, G. J. Brown, C. L. Tung and W. J. Wang, J. Appl. Phys. **107**, 083112 (2010).

2.6 Optimization of InAs/InGaSb superlattice material for very long wavelength infrared detection

H. J. Haugan[a], G. J. Brown[a], M. Kim[a], K. Mahalingam[a], S. Elhamri[b], W. C. Mitchel[a], and L. Grazulis[a]
[a]Air Force Research Laboratory, Wright-Patterson Air Force Base, Ohio 45433, USA
[b]Department of Physics, University of Dayton, Dayton, Ohio 45469, USA

ABSTRACT

We report ternary growth studies to develop a largely strained InAs/InGaSb superlattice (SL) material for very long wavelength infrared (VLWIR) detection. We select a SL structure of 47.0 Å InAs/21.5 Å $In_{0.25}Ga_{0.75}Sb$ that theoretically designed for the greatest possible detectivity, and tune growth conditions for the best possible material quality. Since material quality of grown SLs is largely influenced by extrinsic defects such as nonradiative recombination centers and residual background dopings in the grown layers, we investigate the effect of growth temperature (T_g) on the spectral responses and charge carrier transports using photoconductivity and

Distribution Statement A. Approved for public release; distribution unlimited.

temperature-dependent Hall effect measurements. Results indicate that molecular beam epitaxy (MBE) growth process we developed produces a consistent gap near 50 meV within a range of few meV, but SL spectral sensing determined by photoresponse (PR) intensity is very sensitive to the minor changes in T_g. For the SLs grown from 390 to 470 °C, a PR signal gradually increases as T_g increases from 400 to 440 °C by reaching a maximum at 440 °C. Outside this growth window, the SL quality deteriorates very rapidly. All SLs grown for this study were n-type, but the mobility varied in a variety of range between 11,300 and 21 cm^2/Vs. The mobility of the SL grown at 440 °C was approximately 10,000 V/cm^2 with a sheet carrier concentration of $5x10^{11}$ cm^{-2}, but the mobility precipitously dropped to 21 cm^2/Vs at higher temperatures. Using the knowledge we learned from this growth set, other growth parameters for the MBE ternary SL growth should be further adjusted in order to achieve high performance of InAs/InGaSb materials suitable for VLWIR detection.

INTRODUCTION

The development of infrared (IR) detectors that can operate with minimal cooling requirements is important for low weight and low power IR imaging systems [1-3]. In the very long wavelength infrared (VLWIR) band, InAs/InGaSb superlattice (SL) materials are an excellent candidate for infrared photodiodes with cut-off wavelengths beyond 15 μm, especially for operating temperatures above 15K [4]. The most promising material system currently is a largely strained type-II InAs/$In_{1-x}Ga_xSb$ (ternary) superlattice (SL) system [5]. By alloying indium to the GaSb layer, the lattice constant of the InGaSb layer increases. Therefore, the biaxial tension in the InAs layer lowers the conduction band, while the biaxial compression in the InGaSb layer raises the heavy-hole (HH) band. As a result, the very narrow gap can be achieved with larger absorption coefficients enabled by the use of thinner periods in the designs [6], which is not possible in the case of a minimally strained InAs/GaSb (binary) SL system. In addition, an intentionally introduced strain can create a large splitting between the HH and light-hole bands in the SLs; this situation can prevent hole-hole Auger recombination processes. Therefore the Auger limited minority carrier lifetime, detectivity, and the operating temperature can be significantly improved. Grein et. al. [7] demonstrated how a small change in the strain splitting between the uppermost valence bands can create huge differences on their calculated detectivities. For the SLs designed for the same 80 meV gap at 40 K, the electronic band structure of either 49.7 Å InAs/57.0 Å $In_{0.1}Ga_{0.9}Sb$ or 47.0 Å InAs/21.5 Å $In_{0.25}Ga_{0.75}Sb$ SL designs had total lifetimes of either $5x10^{-9}$ or $1.4x10^{-7}$ seconds. This difference led to an ideal device detectivity of either $5.2x10^{13}$ or $6.0x10^{14}$ $cmHz^{½}$/W, which is an order of magnitude improvement in performance. Therefore, from a theoretical prospective, a largely strained InAs/InGaSb SL system appears to be the best choice for VLWIR detection. Despite the predicted theoretical advantages, and the early focus on ternary SL designs, MBE growth studies on InAs/InGaSb SL materials are not as well developed as for the binary SL materials. A majority of reported VLWIR photodiodes covering 50 % cutoff wavelengths from 15 to 26 μm in the previous years were based on minimally strained binary SL materials [8-11]. The use of a ternary alloy layer can lead to a higher degree of disorder during epitaxial deposition causing alloy scattering, indium segregation, and compositional inter-mixing. Therefore controlling an alloy composition to produce a precise gap and controlling a growth process to achieve a high quality material during a ternary material growth can be more difficult than during a binary material growth. Although there was a report of a ternary SL photodiode with a 50 % cutoff wavelength of 21 μm at 40 K using a 29 MLs InAs/10 MLs $In_{0.07}Ga_{0.93}Sb$ SLs with 1 ML of

Distribution Statement A. Approved for public release; distribution unlimited.

InSb-like interfacial bonds [12], the authors added very little indium to their design and could not take full advantage of the potential strain benefits. The reported detectivity was only $3x10^9$ $cmHz^{½}/W$ at 40 K for this photodiode so the opportunity for significant improvements remains.

In this work, using a combination of high-resolution X-ray diffraction (HRXRD), high-resolution transmission electron microscopy (HRTEM), atomic force microscopy (AFM), photoconductivity, and temperature dependent Hall effects measurements, we develop a molecular beam epitaxy (MBE) growth process specifically for the ternary material growth. We selected a SL structure of 47.0 Å InAs/21.5 Å $In_{0.25}Ga_{0.75}Sb$ proposed by Grein et. al. [7], where their layer thicknesses and indium composition were theoretically adjusted for the greatest possible detectivity, and then optimize growth conditions to be suitable for the ternary material growth. Since SL material quality is strongly coupled with the densities of nonradiative SRH recombination centers and the residual doping [13-15], growth parameters such as III/V flux ratio, growth rates of group III elements, group V cracking temperature, and interface shutter sequence were carefully coordinated to minimize the formation of these defects and then we investigate the effect of T_g on SL material quality.

TERNARY SUPERLATTICE GROWTHS

The ternary SL materials were grown by a Varian GEN-II MBE equipped with dual filament SUMO cells for the group III elemental solid sources of Ga and In, and EPI valved cracker cells for the As and Sb. The repeated SL stacks (0.5 μm) and the undoped GaSb buffer layer (0.5 μm) was deposited on lightly doped n-type GaSb (100) wafers, and a series of 47.0 Å InAs/21.5 Å $In_{0.25}Ga_{0.75}Sb$ SL samples were grown at T_g between 390 and 470 °C. To grow the intended sample structure under minimum cross contamination environment of the anion fluxes, the V/III flux ratio was set at a minimum of 3 for both InGaSb and InAs depositions. In order to avoid an excess amount of As-for-Sb exchange that degrades layer qualities [16, 17], we used very slow growth rate for InAs layer deposition to minimize the As-background flux during the SL growth. The growth rate of 1.20, 0.33, and 0.40 Å/s was used for GaSb, InAs, and InSb, respectively. Since monomeric Sb is the species critical to reducing densities of SRH recombination centers in the SL material [18], we set a Sb cracking zone temperature at 950 ºC for the series, which is close to the suggested value by the EPI Model 200 cc Mark V Corrosive Series Valved Cracker and As cracking zone temperature at 900 ºC [19]. Interface between InAs and InGaSb layer was not intentionally controlled in order to compensate the residual strain in the SLs. The net strain of our series varied between +0.2 % and 0.0 %.

RESULTS AND DISCUSSION

Structural Characterization

In order to evaluate structural properties of grown samples, structural parameters such as SL period, SL net strain, strain profiles across interfaces at atomic resolution, and individual layer thickness were retrieved from a combination of HRXRD and HRTEM analysis. Figure 21 shows a typical diffraction pattern of a closely lattice matched 47.0 Å InAs/21.5 Å $In_{0.25}Ga_{0.75}Sb$ SL structure, showing well defined satellite peaks and Pendellösung fringes around the satellite peaks that demonstrate structurally high quality. To determine the SL period, the spacing between the SL satellite peaks was used. The period was measured to be 68.3 Å which is very close to the intended period of 68.5 Å.

Distribution Statement A. Approved for public release; distribution unlimited.

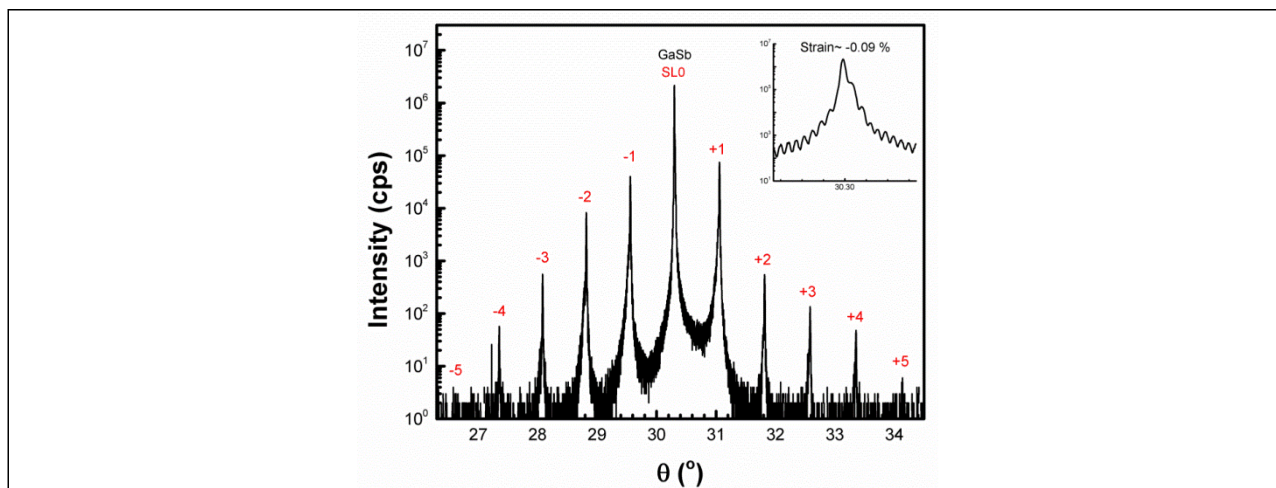

Figure 21. An X-ray diffraction patterns of a closely lattice matched 68.4 Å period ternary superlattice (SL) sample containing a 0.5 µm thick 47.0 Å InAs/21.5 Å $In_{0.25}GaSb_{0.75}Sb$ SLs. This structure produced the band gap of 46.4 meV or a corresponding onset wavelength of 26.7 µm.

While the SL periods can be accurately determined by HRXRC, it is difficult to measure individual layer thickness and alloy composition with this technique. Therefore, we use HRTEM images to retrieve these structural parameters to verify our intended ternary structure. The observations were performed using an aberration (image) corrected Titan 80-300 TEM, which permits the SLs to be imaged at high spatial resolution (≈ 1Å), with negligible delocalization artifacts at interfaces. Figure 22 is a typical HRTEM image of a closely lattice matched ternary SL structure showing the first few SL periods adjacent to the substrate, wherein the amplitude contrast is optimized to delineate the individual layers in the structure. The inset is a magnified image showing that the individual atomic columns are clearly resolved. The average values for the individual layer thicknesses of InAs and InGaSb measured from this image were 45.7 Å ± 0.4 Å and 22.8 Å ± 1.6 Å respectively, which are close to their respective intended values of 47.0 Å and 21.5 Å.

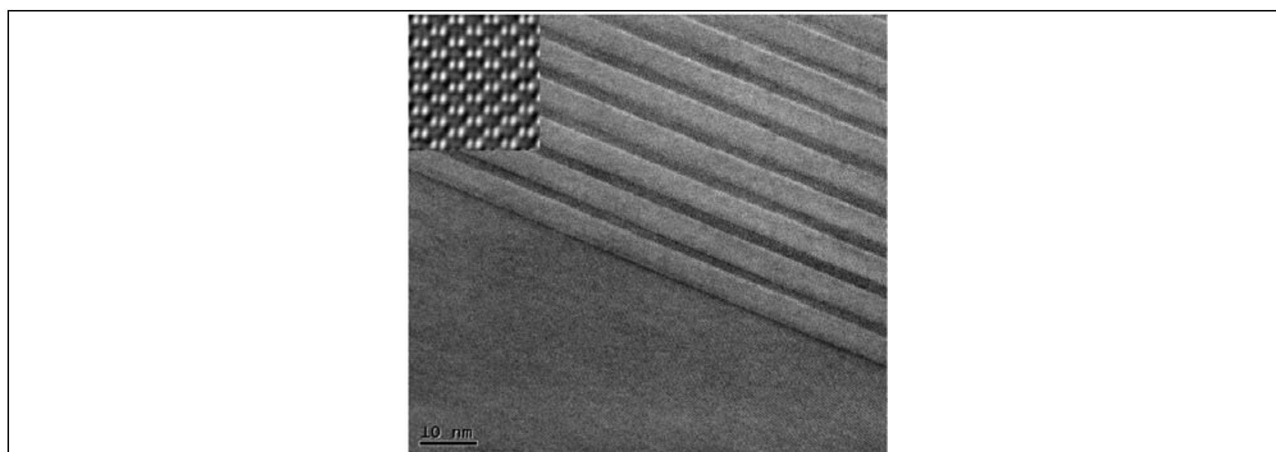

Figure 22. A HRTEM image of a 47.0 Å InAs/21.5 Å $In_{0.25}GaSb_{0.75}Sb$ superlattices showing the first few layers near the substrate. Inset is a magnified image showing the projected atomic columns along the [011] direction.

Distribution Statement A. Approved for public release; distribution unlimited.

In Figure 22 it is interesting to note the presence of distinct bright contrast at local regions near the InGaSb-on-GaSb interfaces, which is not observed at the InAs-on-InGaSb interfaces. To further examine the nature of these interfaces a detailed HRTEM study was performed, wherein the local strain distribution across individual layers in SL was examined using techniques described in recent reports [20, 21]. The inset in Figure 22 is a HRTEM image where the bright spots correspond to the atomic positions. The image clearly shows that the positions are well separated to permit quantitative analysis of atomic displacements within the SL. The analysis was performed such that the strain components ε_{xx} was parallel to the interface (along [011]) and ε_{yy} along the growth direction ([100]).

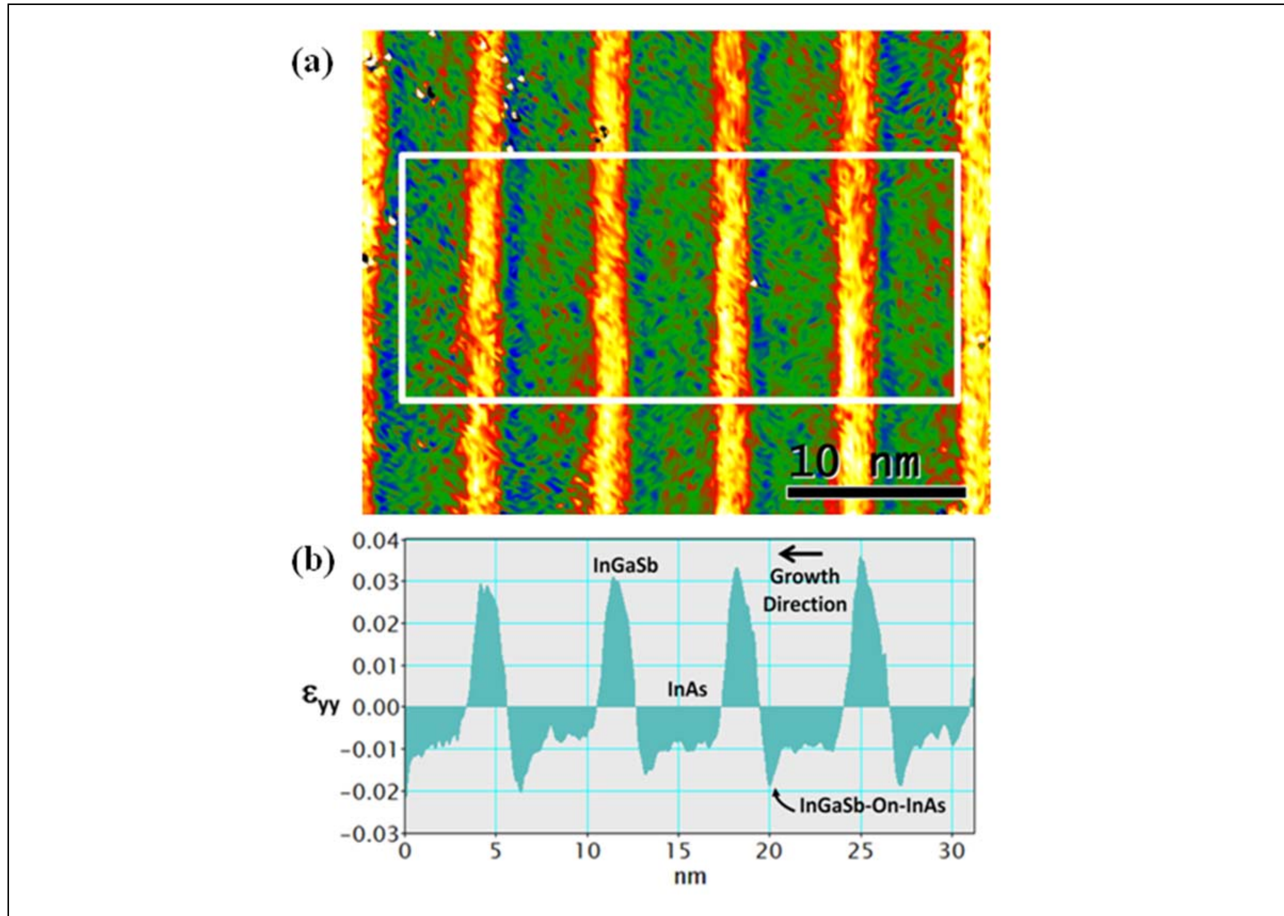

Figure 23. (a) The strain map of an InAs/$In_{0.25}Ga_{0.75}Sb$ superlattices and (b) the strain profile of the strain tensor ε_{yy} along the growth direction averaged parallel to the interface within the white box in (a).

Figure 23a is a map of ε_{yy}, and Figure 23b is a profile of its distribution across individual layers, averaged parallel to the interface within the area indicated in the figure. The strain profile (Figure 23b) clearly shows sharp negative spikes at the InGaSb-on-InAs interface corresponding to the dark blue regions in the strain map in Figure 23a, thereby indicating that this interface is in tensile strain and that the dominant bond type at this interface is Ga-As. It is also observed that the InGaSb layers (bright yellow regions) exhibit a strong compressive strain (approximately 0.03), which is induced by the high indium content in this sample. Further analysis indicated

Distribution Statement A. Approved for public release; distribution unlimited.

that the net strain over several periods examined is to be about 0.0005, which is a closely lattice matched. For the strain balanced SL structure, with a measured period of 68.4 Å, we obtained the band gap energy of 45.3 meV, or a corresponding onset wavelength of 26.4 µm. A summary of the measured HRXRD SL period, net strains, and measured band gap energy determined from the onset of the photoresponse spectra is plotted in Figure 24. This figure demonstrates the repeatability of our MBE growth process over multiple sample depositions, the average period of grown samples was in the 68.0 Å ± 0.5 Å, which is very close to the intended SL period of 68.5 Å. The measured SL structures of the 68.0 Å ± 0.5 Å could produce fairly consistent gap around 50 ± 5 meV.

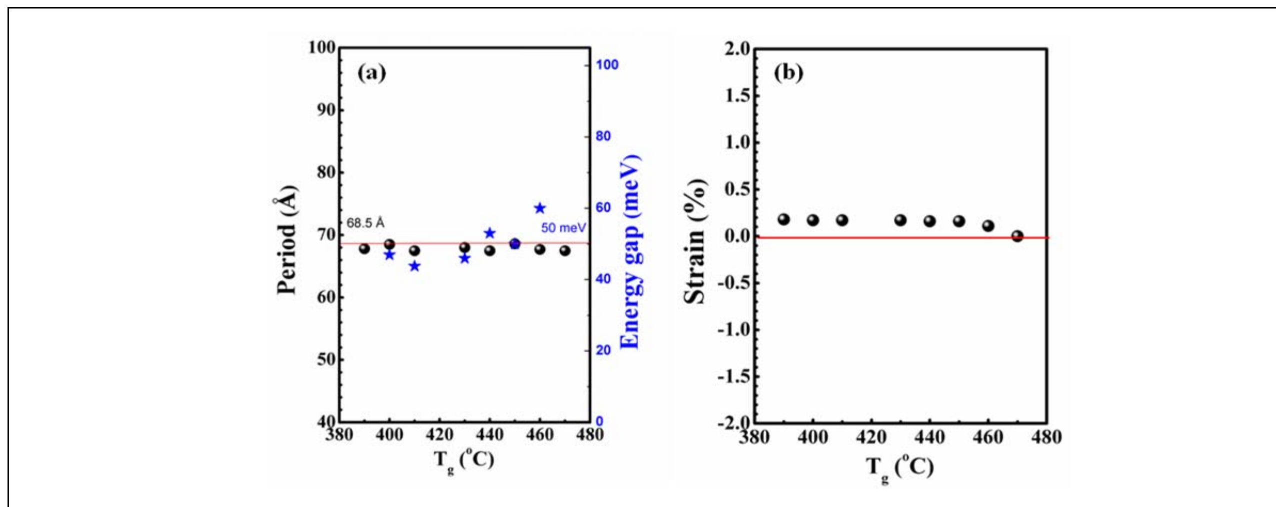

Figure 24. (a) The measured period (black circles) and measured band gap (blue stars), (b) measured net strain (black circles) as a function of the growth temperature (T_g).

Surface Characterization

In order to evaluate the surface morphology of epitaxial samples, the surface roughness and the number of defects, as well as the size and shape, were monitored by AFM images scanned over 50 µm x 50 µm areas. Figure 25 shows the images of a few selected SL samples that were grown at the respective growth temperatures of 390, 400, 440, 460, and 470 ºC. Despite the large difference in the growth temperatures, there were no significant changes in the average root-mean-square (RMS) roughness for the SL samples grown at T_g from 400 to 460 ºC. In this temperature range, the RMS values were around 3 Å. However, there were significant changes in RMS values for the two SL samples grown at the lowest (390 ºC) and the highest temperature (470 ºC), their respective RMS values were 21 and 65 Å.

Distribution Statement A. Approved for public release; distribution unlimited.

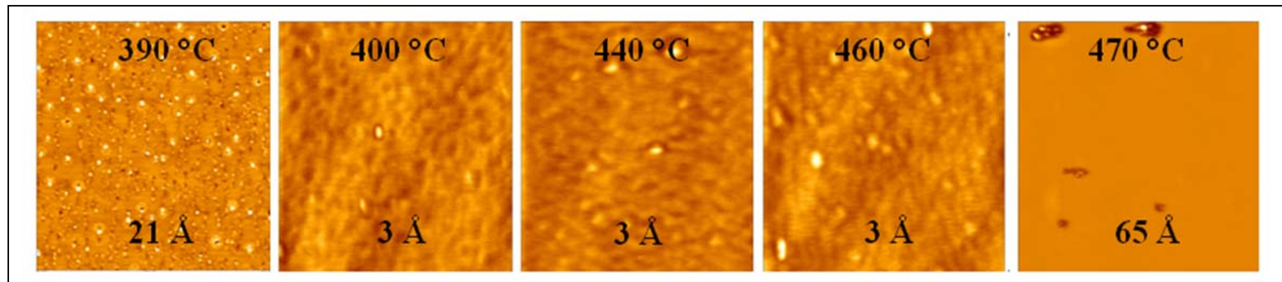

Figure 25. AFM images of 50 µm x 50 µm area scans of 0.5 µm thick 47.0 Å InAs/21.5 Å $In_{0.25}Ga_{0.75}Sb$ superlattices grown at growth temperature (T_g) of 390-470 ºC (from left to right). The value listed on the top (the bottom) of each image represents a T_g (an average root-mean-square roughness).

Optical Characterization

Since the strength of the PR signal is a strong indication of the suitability of a material for infrared sensing, PR spectra were used to determine the band gap and the strength of the optically excited signal. The spectra were collected with a Fourier Transform Infrared Spectrometer at a temperature of 10 K. Due to the relatively low resistivity of the samples, the photoconductivity was measured in the current biased mode, with a current of 0.5 mA between two parallel strip contacts on the surface. Figure 26a shows the five PR spectra collected from the sample set with varying T_g of 400, 410, 430, 440, and 450 ºC. Although the PR intensities are given in arbitrary units, the relative signal strengths can still be compared as the test conditions for all the samples were kept constant. We observe that the band gap energies of all SLs in this series were consistently around 50 ±5 meV as shown in the Figure 24a. The PR intensity measured at 100 meV above the band gap gradually increases as T_g increases from 400 to 440 ºC, reaching a maximum at 440 ºC, and then drops by over an order of magnitude at higher temperatures (see Figure 26b). Thus, there is a relatively narrow growth window of 410-440 ºC for the group V fluxes and cracking zone temperatures used. Outside this temperature window, the material quality deteriorates very rapidly. The measured band gap energies from all of the grown SL ternary samples were approximately 30 meV lower than the theoretically predicted value of 80 meV by Grein et. al. [7], and the cutoff wavelength of 19 µm, measured at the point where the PR intensity has dropped by 50%, was longer. Although the HRXRD and HRTEM measurements verify that the SL samples grown were very close to the intended design, there remains a discrepancy between theory and experiment that needs to be resolved. Overall, a good photoresponse signal was measured despite the fact that the SL total thickness was only 0.5 µm. The heavy fringing on the long wavelength portion of the spectrum is not noise but a result of multiple internal reflections through the substrate/buffer/superlattice stack. The lightly n-type GaSb wafers do have significant infrared transparency [22]. As shown in Figure 26, the SL has its maximum response over a wide wavelength range up to ~15 µm.

Distribution Statement A. Approved for public release; distribution unlimited.

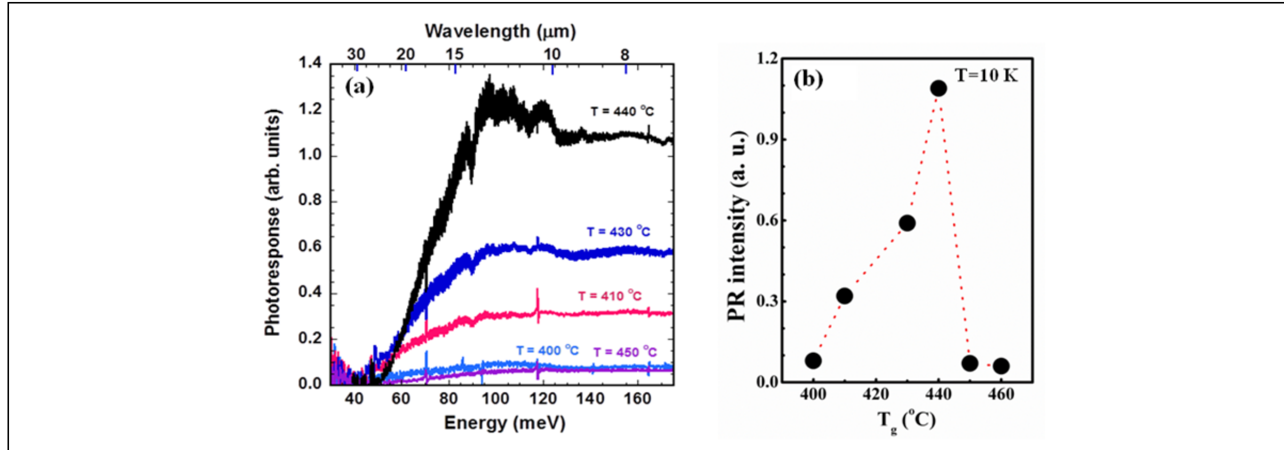

Figure 26. (a) Comparison of the photoresponse spectra of five 47.0 Å InAs/21.5 Å $In_{0.25}Ga_{0.75}Sb$ SL samples grown at 400-450 °C. (b) The plot shows the PR intensity as a function of growth temperature (T_g).

Electrical Characterization

Hall measurements are normally used to characterize semiconductor materials. The best SL materials are grown on GaSb substrates, where lattice mismatch induced dislocations are at a minimum. However, standard GaSb substrates are conductive and traditional Hall measurements have difficulty separating the conductivity of the SL from that of the substrate at temperatures above about 20K. Recently, lightly doped n-type GaSb substrates have become available with significantly reduced absorption in the infrared spectrum [22]. For SLs grown on these types of substrates, we were able to significantly reduce the contribution from the substrate. This reduction in the contribution from the substrate allows for the use of traditional in-plane Hall measurements as a measure of material quality needed for device performance [14]. Here we report transport parameters, carrier density and mobility, obtained by variable temperature resistivity and Hall effect measurements for SL samples deposited on lightly doped n-type GaSb substrates. The temperature dependence of the carrier density and in-plane mobility for two SLs is shown in Figure 27, where the mobility and carrier density are relatively temperature insensitive up to roughly 70 K, which is significantly higher than the 20 K observed for most previous SL samples deposited on the p-type GaSb substrates [23, 24]. The 10 K carrier density and mobility, along with the corresponding T_g, for each sample are summarized in Table 3.

Distribution Statement A. Approved for public release; distribution unlimited.

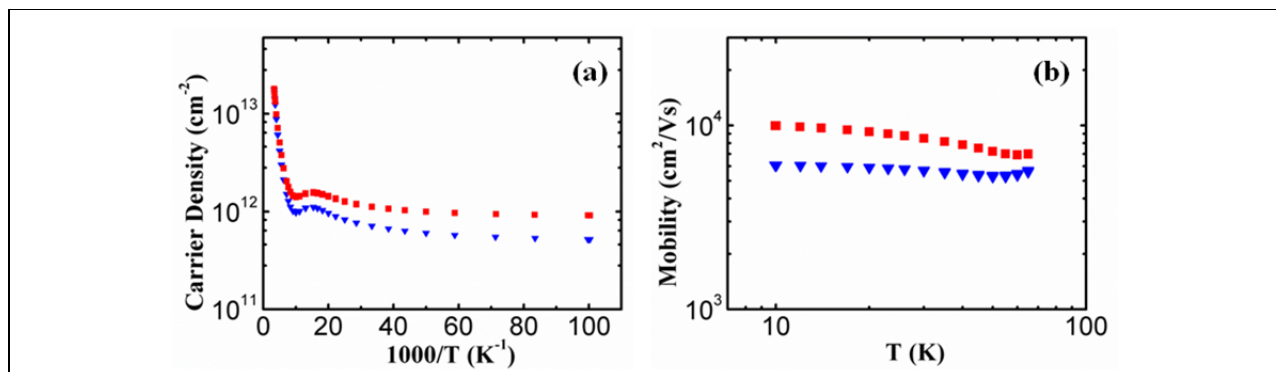

Figure 27. Temperature dependence of (a) the carrier density as a function of 1000/T and (b) the carrier mobility as a function of measurement temperature for SL samples grown at 440 (red solid squares) and 390 °C (blue solid triangles).

Table 3. Summary of the measurements results for the sample set. The photoresponse and Hall results are from measurements at 10 K. The cut-off wavelength λ_c is selected at the point where the intensity drops by 50 %. The PR intensity was measured at 100 meV above the band gap. All of the samples were n-type. The average root-mean-square roughness was based on AFM images of 50 x 50 μm^2 area scan.

Sample	T_g (°C)	P (Å)	ε (%)	E_g (meV)	λ_c (μm)	RMS (Å)	PR intensity (arb. units)	Conc. (x10^{11}cm^{-2})	Mobility (cm^2/Vs)
SL1	390	67.8	+0.18	X	X	21	X	9.1	6073
SL2	400	68.5	+0.17	47.0	19.0	3	0.08	8.9	9887
SL3	410	67.5	+0.17	43.8	20.1	5	0.32	7.1	11286
SL4	430	68.0	+0.17	46.0	19.0	5	0.59	6.4	10502
SL5	440	67.5	+0.16	53.0	17.0	3	1.09	5.2	9950
SL6	450	68.6	+0.16	50.0	16.2	3	0.07	5.6	8529
SL7	460	67.7	+0.11	60.0	15.7	3	0.06	280	112
SL8	470	67.5	+0.00	X	X	65	X	1200	21

The impact of growth temperature on the carrier density and carrier mobility measured at 10 K is illustrated in Figure 28. The mobility (carrier density) increases (decreases) from 6,000 (9 x 10^{11} cm^{-2}) to 11,300 cm^2/Vs (7 x 10^{11} cm^{-2}) as T_g increases from 390 to 410 ºC, gradually decreases to 8,500 cm^2/Vs (~5 x 10^{11} cm^{-2}) as T_g increases to 450 ºC, and then drops (increases) significantly for the two highest T_g of 460 and 470 ºC. The background carrier density gradually decreases, reaching a minimum of 5.2 x 10^{11} cm^{-2} at 440 ºC, with a corresponding mobility of roughly 10,000 cm^2/Vs. Based on the transport data, transport properties rapidly deteriorate for T_g above 450 ºC.

Distribution Statement A. Approved for public release; distribution unlimited.

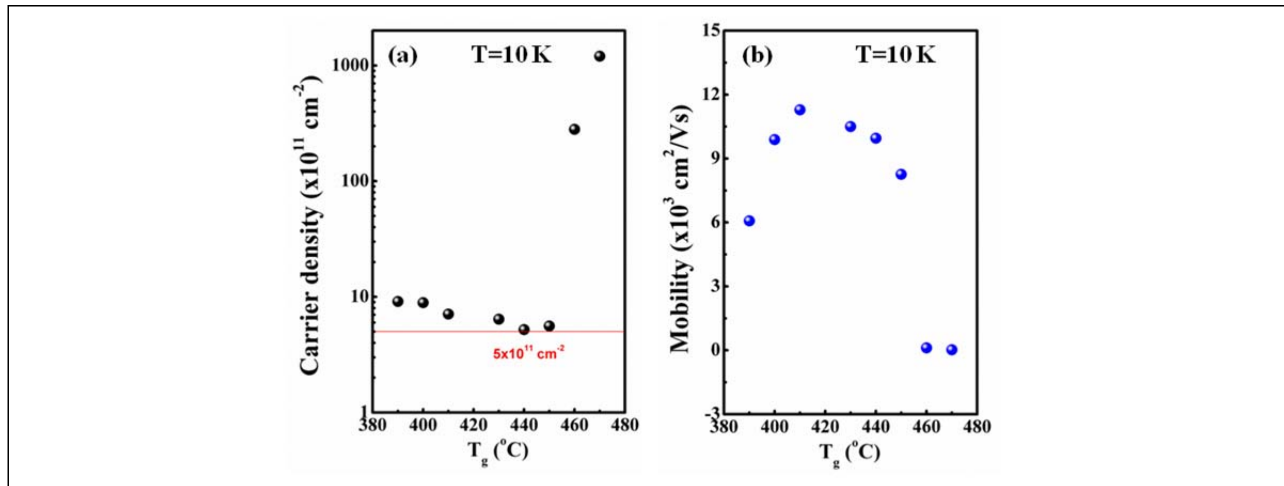

Figure 28. (a) The carrier density and (b) the mobility as a function of growth temperature measured at 10 K.

CONCLUSIONS

In conclusion, a combination of high-resolution X-ray rocking curve, high-resolution transmission electron microscopy, atomic force microscopy, photoconductivity, and temperature dependent Hall effect measurements was used to investigate the impact of T_g on the material quality of VLWIR InAs/InGaSb SLs. For the studies, a series of 47.0 Å InAs/21.5 Å $In_{0.25}Ga_{0.75}Sb$ SLs were grown by MBE at T_g ranging from 390 to 470 °C. The results showed that our MBE growth process used to create a ternary SL structure produced a consistent band gap of 50 ± 5 meV. However the material quality of the grown samples, as assessed by various measurement techniques, was very sensitive to T_g. We observed a general trend of improving PR intensity as the growth temperature increases. The PR signal exhibited a maximum for the growth temperature of 440 °C, and then dropped rapidly to less than 0.1 a. u. at higher temperatures. The SLs were all residual n-type, but the mobility varied between 11,300 and 21 cm^2/Vs. The mobility of the SL grown at 440 °C was approximately 10,000 V/cm^2 with a sheet carrier concentration of 5x10^{11} cm^{-2}, but the mobility precipitously dropped to 21 cm^2/Vs at higher temperatures. Average surface roughness of SL samples that produce strong PR signals was around 3 Å and a quantitative analysis of the strain distribution performed at the atomic scale by aberration corrected TEM provided valuable information about strain distribution at the InGaSb-on-InAs interfaces in the superlattices examined in this study. A strong compressive strain of approximately 0.03 induced by InGaSb alloyed layers was compensated by tensile strains created by Ga-As bonds at the InGaSb-on-InAs interface along with the InAs layers.

REFERENCES

[1] A. Rogalski, Infrared Phys. Technol. **50**, 240 (2007).

[2] L. Becker, Proc. SPIE **6127**, 61270S (2006).

[3] T. Ashley and N. T. Gorden, Proc. SPIE **5359**, 89 (2004).

[4] A. Rogalski, Progress in Quantum Electronics **27**, 59 (2003).

[5] D. L. Smith and C. Mailhiot, J. Appl. Phys. **62**, 2545 (1987).

[6] H. Kroemer, Physica E **20**, 196 (2004).

Distribution Statement A. Approved for public release; distribution unlimited.

[7] C. H. Grein, W. H. Lau, T. L. Harbert, and M. E. Flatté, Proc. SPIE **4795**, 39 (2002).

[8] Y. Wei, A. Gin, M. Razeghi, and G. J. Brown, Appl. Phys. Lett. **80**, 3262 (2002).

[9] H. Mohseni, Y. Wei, and M. Razeghi, Proc. SPIE **4288**, 191 (2001).

[10] Y. Wei, A. Gin, M. Razeghi, and G. J. Brown, Appl. Phys. Lett. **81**, 3675 (2002).

[11] H. Mohseni, M. Razeghi, G. J. Brown, and Y. S. Park, Appl. Phys. Lett. **78**, 2107 (2001).

[12] E. H. Aifer, E. M. Jackson, G. Boishin, L. J. Whitman, I. Vurgaftman, J. R. Meyer, J. C. Culbertson, and B. R. Bennett, Appl. Phys. Lett. **82**, 4411 (2003).

[13] H. J. Haugan, S. Elhamri, F. Szmulowicz, B. Ullrich, G. J. Brown, and W. C. Mitchel, Appl. Phys. Lett. **92**, 071102 (2008).

[14] H. J. Haugan, S. Elhamri, G. J. Brown, and W. C. Mitchel, J. Appl. Phys. **104**, 073111 (2008).

[15] H. J. Haugan, S. Elhamri, W. C. Mitchel, B. Ullrich, G. J. Brown, L. Grazulis, and S. Houston, Proc. SPIE **7222,** 722220Y (2009).

[16] E. M. Jackson, G. I.Boishin, E. H. Aifer, B. R. Bennett, L. J. Whitman, J. Crys. Growth **270**, 301 (2004).

[17] B. Z. Nosho, B. B. Bennett, L. J. Whitman, and M. Goldenberg, J. Vac. Sci. Technol. B **19**, 1626 (2001).

[18] R. H. Miles, D. H. Chow, Y.-H. Zhang, P. D. Brewer, and R. G. Wilson, Appl. Phys. Lett. **66**, 1921 (1995).

[19] H. J. Haugan, G. J. Brown, S. Elhamri, W. C. Mitchel, K. Mahalingam, M. Kim, G. T. Noe, N. E. Ogden, and J. Kono, Appl. Phys. Lett. **101**, 171105 (2012).

[20] K. Mahalingam, H. J. Haugan, G. J. Brown, K. G. Eyink, and Bin Jiang Proc. SPIE **8268**, 826831 (2012).

[21] K. Mahalingam, H. J. Haugan, G. J. Brown, K. G. Eyink, Ultramicroscopy (2012 in press), http://dx.doi.org/10.1016/j.ultramic.2012.09.005.

[22] L. P. Allen, P. Flint, G. Dallas, D. Bakken, K. Blanchat, G. J. Brown, S. R. Vangala, W. D. Goodhue, and K. Krishnaswami, Proc. SPIE **7298**, 72983P (2009).

[23] H. J. Haugan, G. J. Brown, F. Szmulowicz, S. Elhamri, AIP Conf. Proc. **1416**, 155 (2011).

[24] H. J. Haugan, G. J. Brown, F. Szmulowicz, S. Elhamri, B. V. Olson, T. F. Boggess, L. Grazulis, Proc. SPIE **8154**, 81540J (2011).

Distribution Statement A. Approved for public release; distribution unlimited.

3.0 PUBLICATIONS

3.1 Refereed Journal Articles

"Optical and Electrical Quality Improvements of Undoped InAs/GaSb Superlattices", H. J. Haugan, B. Ullrich, L. Grazulis, S. Elhamri, G. J. Brown and W. C. Mitchel, J. Vac. Sci. Technol. B **28**, C3C19 (2010).

"Magneto-optics of InAs/GaSb Superlattices", H. J. Haugan, B. Ullrich, S. Elhamri, F. Szmulowicz, G. J. Brown, L. C. Tung, and Y. J. Wang, J. Appl. Phys. **107**, 083112 (2010).

"Transport Studies of MBE-grown InAs/GaSb Superlattices", F. Szmulowicz, H. J. Haugan, S. Elhamri, G. J. Brown and W. C. Mitchel, Opto-electronics Review **18**, 60 (2010).

"GaSb for passivating type-II InAs/GaSb", F. Szmulowicz and G. J. Brown, Infrared Physics & Technology **53**, 305 (2010).

"Effect of Interfacial Formation on the Properties of Very Long Wavelength Infrared InAs/GaSb Superlattices", H. J. Haugan, G. J. Brown and L. Grazulis, J. Vac. Sci. Technol. **B 29**, 03C101-1 (2011).

"Calculation of the Vertical and Horizontal Electron Mobilities in InAs/GaSb Superlattices", F. Szmulowicz and G. J. Brown, Appl. Phys. Lett. **98**, 182105 (2011).

"Calculation of Vertical and Horizontal Mobilities in InAs/GaSb Superlattices", F. Szmulowicz, H. J. Haugan, S. Elhamri and G. J. Brown, Phys. Rev. B **84**, 155307 (2011).

"Coherent Phonon Dynamics in Short-period InAs/GaSb Superlattices", G. T. Noe, H. J. Haugan, G. J. Brown, G. D. Sanders, C. J. Stanton and J. Kono, Superlattices and Microstructures **52**, 1071 (2012).

"InAs MOS Devices Passivated with MBE-grown Gd_2O_3 Dielectrics", C. Lin, P.-C. Chiu, M. L. Huang, H.-K. Lin, T. H. Chiang, W. C. Lee, Y. C. Chang, Y. H. Chang, J.-I. Chyi, G. J. Brown, J. Kwo and M. Hong, J. Vac. Sci. & Technol. B **30**, 02B118-1(2012).

"Post Growth Annealing Study on LWIR InAs/GaSb Superlattices", H. J. Haugan, G. J. Brown, S. Elhamri, S. Pacley, B. V. Olson and T. F. Boggess, J. Appl. Phys. **111**, 053113 (2012).

"Strain Analysis of Compositionally Tailored Interfaces in InAs/GaSb Superlattices by Aberration Corrected Transmission Electron Microscopy", K. Mahalingam, H. J. Haugan, G. J. Brown and K. E. Eyink, Microscopy & Microanalysis **18** (S2), 1808 (2012).

"Impact of Growth Temperature on InAs/GaInSb Strained Layer Superlattices for Very Long Wavelength Infrared Detection", H. J. Haugan, G. J. Brown, S. Elhamri, W. C. Mitchel, K. Mahalingam, M. Kim, G. T. Noe, N. E. Ogden and J. Kono, Appl. Phys. Lett **101**, 171105 (2012).

"Calculation of the Temperature Dependence of the Vertical and Horizontal Mobilities in InAs/GaSb Superlattices", F. Szmulowicz, H. J. Haugan, S. Elhamri and G. J. Brown, Infrared Phys. & Technol. **56**, 76 (2013).

Distribution Statement A. Approved for public release; distribution unlimited.

"Quantitative Analysis of Interfacial Strain in InAs/GaSb Superlattices by Aberration Corrected HRTEM and HAADF-STEM", K. Mahalingam, H. J. Haugan, G. J. Brown and K. G. Eyink, Ultramicroscopy **127**, 70 (2013).

"Calculation of Interface Roughness Scattering-limited Vertical and Horizontal Mobilities in InAs/GaSb Superlattices as a Function of Temperature", F. Szmulowicz and G. J. Brown, J. Appl. Phys. **113**, 014302 (2013).

"Surface Passivation of GaSb(100) Using Molecular Beam Epitaxy of Y_2O_3 and Atomic Layer Deposition of Al_2O_3 : A Comparative Study", R.-L. Chu, W.-J. Hsueh, T.-H. Chiang, W.-C. Lee, H.-Y. Lin, T.-D. Lin, G. J. Brown, J.-I. Chyi, T.-S. Huang, T.-W. Pi, J. R. Kwo and M. Hong, Appl. Phys. Express **6**, 121201 (2013).

"Strain Analysis of Compositionally Tailored Interfaces in InAs/GaSb Superlattices", K. Mahalingam, H. J. Haugan and G. J. Brown, Appl. Phys. Lett. **103**, 211605 (2013).

"Electrical, Optical and Structural Studies of InAs/InGaSb VLWIR Superlattices", Gail J. Brown, Said Elhamri, William C. Mitchel, Heather J. Haugan, Krishnamurthy Mahalingam, Mu J. Kim and Frank Szmulowicz, in *The Wonder of Nanotechnology: Quantum Optoelectronic Devices and Applications*, M. Razeghi. L. Esaki, and K. von Klitzing, Eds., SPIE Press, Bellingham, WA, pp. 41-58 (2013).

"Optimum Growth Window for InAs/GaInSb Superlattice Materials Tailored for Very Long Wavelength Infrared Detection", H. J. Haugan, G. J. Brown, K. Mahalingam, L. Grazulis, G. T. Noe, N. E. Ogden, and J. Kono, J. Vac. Sci. Technol. B **32**, 02C109-1 (2014).

3.2 Conference Proceedings

"Composition and Strain Mapping of Interfaces in InAs/GaSb Superlattices by Aberration-corrected high-resolution Transmissiion Electron Microscopy", K. Mahalingam, H. J. Haugan, G. J. Brown, K. G. Eyink, F. Szmulowicz, B. Jiang, C. F. Kisielowski, *Quantum Sensing and Nanophotonic Devices VII*, Manijeh Razeghi, Rengarajan Sudharsanan, Gail J. Brown, Editors, SPIE Proc. **7608**, 76081S (2010).

"Type-II Superlattice Materials Research at the Air Force Research Laboratory", G. J. Brown, S. Elhamri, H. E. Smith, K. Mahalingam, H. J. Haugan, S. Pacley, B. Ullrich and F. Szmulowicz, *Infrared Technology and Applications XXXVI*, Bjorn F. Andresen, Gabor F. Fulop, Paul R. Norton, Editors, SPIE Proc. **7660**, 76603P (2010).

"Vertical Transport in InAs/GaSb Superlattices: Model Results and Relation to In-plane Transport", F. Szmulowicz and G. J. Brown, *Quantum Sensing and Nanophotonics VIII*, Manijeh Razeghi, Rengarajan Sudharsanan and Gail J Brown, Editors, SPIE Proc. **7945**, 79451U (2011).

"100 mm Diameter GaSb Substrates with Extended IR Wavelength for Advanced Space Based Applications", L. P. Allen, J. P. Flint, G. Meschew, G. Dallas, D. Bakken, G. J. Brown, A. Khoshakhlagh and C. J. Hill, *Infrared Technology and Applications XXXVII*, Bjorn F. Andresen, Gabor F. Fulop, Paul R. Norton, Editors, SPIE Proc. **8012**, 801215 (2011).

Distribution Statement A. Approved for public release; distribution unlimited.

"The Role of InAs Thickness on the Material Properties of InAs/GaSb Superlattices", H. J. Haugan, G. J. Brown, F. Szmulowicz, S. Elhamri, B. V. Olson, T. F. Boggess and L. Grazulis, *Infrared Remote Sensing and Instrumentation XIX*, Marija Strojnik and Gonzalo Paez, Editors, SPIE Proc. **8154**, 815417 (2011).

"Design Effects on the Material Properties of InAs/GaSb Superlattices", H. J. Haugan, G. J. Brown, F. Szmulowicz and S. Elhamri, *15th International Conference on Narrow Gap Systems (NGS15)*, AIP Conf. Proc. **1416**, 155 (2011).

"Quantitative Strain Analysis of Interfaces in InAs/GaSb Superlattices by Aberration-corrected HAADF-STEM", K. Mahalingam, H. J. Haugan, G. J. Brown, K. G. Eyink and B. Jiang, *Quantum Sensing and Nanophotonic Devices IX*, Manijeh Razeghi, E. Tourné and Gail J Brown, Editors, SPIE Proc. **8268**, 826831-1 (2012).

"Post Growth Annealing Study on LWIR InAs/GaSb Superlattices", H. J. Haugan, G. J. Brown, S. Elhamri, S. Pacley, B. V. Olson, T. F. Boggess, *Infrared Sensors, Devices, and Applications II*, Editors, Paul D. LeVan, Ashok K. Sood, Priyalal S. Wijewarnasuriya, and Arvind I. D'Souza, Editors, SPIE Proc. **8512**, 85120K-1 (2012).

"Exploring Optimum Growth Window for High Quality InAs/InGaSb Superlattice Materials", H. J. Haugan, G. J. Brown, M. Kim, K. Mahalingam, S. Elhamri, W. C. Mitchel and L. Grazulis, *Infrared Technology and Applications XXXIX*, Bjorn F. Andressen, Gabor F. Fulop, Charles M. Hanson, and Paul R. Norton, Editors, SPIE Proc. **8704**, 870413 (2013).

Distribution Statement A. Approved for public release; distribution unlimited.

LIST OF ACRONYMS, ABBREVIATIONS, AND SYMBOLS

Acronym	Definition
VLWIR	Very Long Wavelength Infrared
InAs	Indium Arsenide
InGaSb	Indium Gallium Antimonide
SL	Superlattice
IRS	Interface Roughness Scattering
PR	Photoresponse
HH	Heavy-hole
SRH	Shockley-Read-Hall
T_g	Growth Temperature
HRTEM	High-Resolution Transmission Electron Microscopy
HRXRC	High-Resolution X-ray Rocking Curve
CW	Continuous Wave
ns	Nanosecond
MWIR	Mid-Wavelength Infrared
As	Arsenic
STEM	Scanning Transmission Electron Microscopy
HAADF	High-angle Annular Dark-field
IR	Infrared
HRXRD	High-Resolution X-ray Diffraction
AFM	Atomic Force Microscopy
MBE	Molecular Beam Epitaxy
RMS	Root-Mean-Square

Distribution Statement A. Approved for public release; distribution unlimited.
Approved by 88ABW Public Affairs Office: Case number 88ABW-2015-1224 on 19-MAR-2015.